Cell Reports

Resource

Metabolic Maturation Media Improve Physiological Function of Human iPSC-Derived Cardiomyocytes

Graphical Abstract

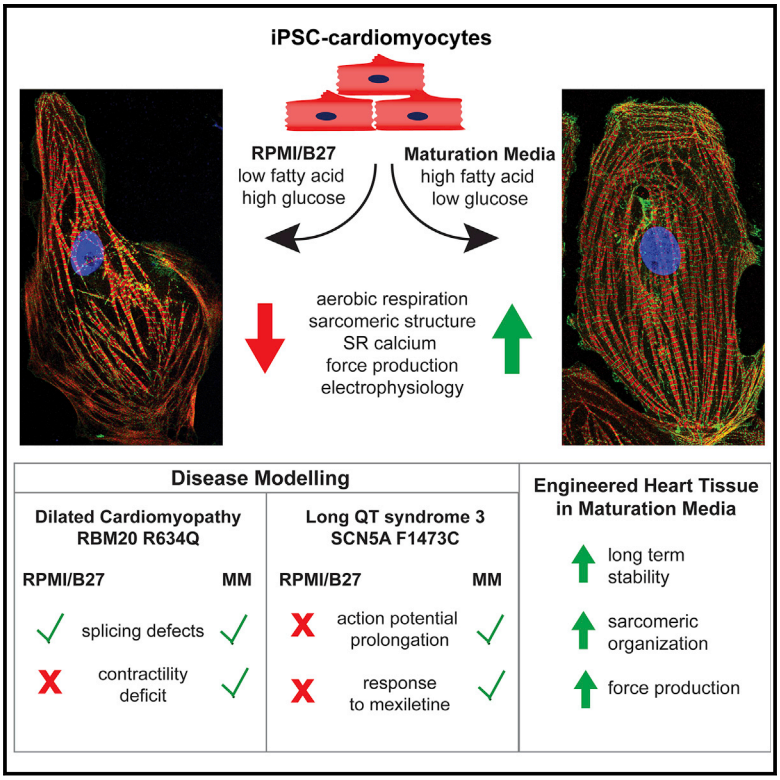

Authors

Dries A.M. Feyen, Wesley L. McKeithan, Arne A.N. Bruyneel, ..., Thomas Eschenhagen, Christian M. Metallo, Mark Mercola

Correspondence

mmercola@stanford.edu

In Brief

Physiological immaturity of iPSC-derived cardiomyocytes limits their fidelity as disease models. Feyen et al. developed a low glucose, high oxidative substrate media that increase maturation of ventricular-like hiPSC-CMs in 2D and 3D cultures relative to standard protocols. Improved characteristics include a low resting V_m, rapid depolarization, and increased Ca^{2+} dependence and force generation.

Highlights

- We developed a defined maturation medium for hiPSC-CMs
- The media improve electrophysiological and mechanical characteristics of hiPSC-CMs
- The media improve the fidelity of disease modeling

Feyen et al., 2020, Cell Reports *32*, 107925
July 21, 2020
https://doi.org/10.1016/j.celrep.2020.107925

CellPress

Cell Reports

CellPress
OPEN ACCESS

Resource

Metabolic Maturation Media Improve Physiological Function of Human iPSC-Derived Cardiomyocytes

Dries A.M. Feyen,[1,2,8] Wesley L. McKeithan,[1,3,4,8] Arne A.N. Bruyneel,[1,8] Sean Spiering,[3,4] Larissa Hörmann,[5] Bärbel Ulmer,[5] Hui Zhang,[4] Francesca Briganti,[1] Michaela Schweizer,[6] Bence Hegyi,[7] Zhandi Liao,[7] Risto-Pekka Pölönen,[7] Kenneth S. Ginsburg,[7] Chi Keung Lam,[1] Ricardo Serrano,[1] Christine Wahlquist,[1,3,4] Alexander Kreymerman,[1] Michelle Vu,[1] Prashila L. Amatya,[1] Charlotta S. Behrens,[5] Sara Ranjbarvaziri,[1] Renee G.C. Maas,[1,2] Matthew Greenhaw,[1] Daniel Bernstein,[1] Joseph C. Wu,[1] Donald M. Bers,[7] Thomas Eschenhagen,[5] Christian M. Metallo,[4] and Mark Mercola[1,3,4,9,*]

[1]Cardiovascular Institute and Department of Medicine, Stanford University, Stanford, CA 94305, USA
[2]Department of Cardiology, University Medical Center Utrecht, Utrecht, the Netherlands
[3]Sanford-Burnham-Prebys Medical Discovery Institute, La Jolla, CA, USA
[4]Department of Bioengineering, University of California, San Diego, San Diego, CA, USA
[5]Institute of Experimental Pharmacology and Toxicology, University Medical Center Hamburg-Eppendorf, Hamburg, Germany
[6]Electron Microscopy Unit, Center for Molecular Neurobiology Hamburg, University Medical Center Hamburg-Eppendorf, Hamburg, Germany
[7]Department of Pharmacology, University of California, Davis, Davis, CA, USA
[8]These authors contributed equally
[9]Lead Contact
*Correspondence: mmercola@stanford.edu
https://doi.org/10.1016/j.celrep.2020.107925

SUMMARY

Induced pluripotent stem cell-derived cardiomyocytes (iPSC-CMs) have enormous potential for the study of human cardiac disorders. However, their physiological immaturity severely limits their utility as a model system and their adoption for drug discovery. Here, we describe maturation media designed to provide oxidative substrates adapted to the metabolic needs of human iPSC (hiPSC)-CMs. Compared with conventionally cultured hiPSC-CMs, metabolically matured hiPSC-CMs contract with greater force and show an increased reliance on cardiac sodium (Na^+) channels and sarcoplasmic reticulum calcium (Ca^{2+}) cycling. The media enhance the function, long-term survival, and sarcomere structures in engineered heart tissues. Use of the maturation media made it possible to reliably model two genetic cardiac diseases: long QT syndrome type 3 due to a mutation in the cardiac Na^+ channel SCN5A and dilated cardiomyopathy due to a mutation in the RNA splicing factor RBM20. The maturation media should increase the fidelity of hiPSC-CMs as disease models.

INTRODUCTION

The ability to produce an unlimited supply of human cardiomyocytes from induced pluripotent stem cells (hiPSC-CMs) has allowed the unprecedented ability to model human heart disease *in vitro*. The scalability of hiPSC-CMs makes them amenable for high-throughput phenotypic screening applications in which the role of proteins and signaling pathways can be unraveled in the context of CM physiological function (Bruyneel et al., 2018). Nonetheless, state-of-the-art protocols to generate hiPSC-CMs yield fetal-like CMs with characteristically low sarcoplasmic reticulum (SR) calcium (Ca^{2+}) content and, in many batches, action potentials (APs) that depend on Ca^{2+} rather than sodium (Na^+) currents (Yang et al., 2014a). These physiological characteristics represent barriers to modeling complex adult cardiac physiology and disease and can therefore undermine the relevance of subsequent findings. In this regard, maturation of hiPSC-CMs remains central to unlocking the full potential of this technology.

During fetal development, CM progenitors switch from glycolytic to oxidative metabolism to support the energy demands of functional CMs (Gaspar et al., 2014). This mitochondrial shift is necessary for proper CM development (Hom et al., 2011) and allows CMs to metabolize diverse carbon sources (e.g., fatty acids, ketone bodies, branched-chain amino acids) in order to maintain cardiac function in the face of fluctuating substrate availability in the bloodstream (Kolwicz et al., 2013; Lloyd et al., 2004). In contrast to their fetal counterparts, hiPSC-CMs have deficient fatty acid oxidation (FAO) despite expression of appropriate genes (Zhang et al., 2020).

The most efficient protocols for CM differentiation rely on basal RPMI 1640 media supplemented with B27 that was

originally designed for hippocampal neuronal culture (Lian et al., 2012). Because lipid-poor and glucose-rich media conditions, such as in RPMI/B27 media, can promote *de novo* lipogenesis and suppress FAO (Saggerson, 2008; van Weeghel et al., 2018), we sought to develop media with glucose and oxidative substrates levels adapted to the metabolic needs of CMs. The media contain physiologically appropriate levels of glucose and Ca^{2+} and are supplemented with a complex mixture of albumin-bound fatty acid (AlbuMAX), creatine, L-carnitine, and taurine to support CM energetics. A 3- to 5-week period of directed metabolic maturation increased FAO. Moreover, it also promoted electrophysiological, structural, SR, and mechanical maturation, which suggests a mechanistic association between metabolic status and physiological maturation of CMs. The benefit was also apparent in 3D-engineered heart tissues (EHTs), in which case it enhanced sarcomere structure and function as well as allowed long-term culture. Finally, the maturation protocol enhanced the fidelity of modeling two cardiac disorders: long QT syndrome type 3 (LQT3), which depends on cardiac Na^+ channel activity, and the contractile deficit of RBM20 mutant dilated cardiomyopathy (DCM), which depends on robust Ca^{2+} cycling.

RESULTS

RPMI/B27-based media have become routine in cardiogenic differentiation protocols because they provide excellent support for differentiation and maintenance of iPSC-CMs. However, RPMI/B27-based media have high levels of glucose and low levels of oxidative substrates such as lipids. Using ^{13}C metabolic flux analysis, we observed that under lipid-deficient conditions, iPSC-CMs are unable to oxidize lipids and that lipid supplementation led to a pronounced increase in oxidation of [^{13}C]palmitate and a decrease of glucose oxidation to tricarboxylic acid metabolism (Zhang et al., 2020). To test whether lipid supplementation would increase iPSC-CM maturation and enhance the disease-modeling potential of iPSC-CMs, we formulated media containing a AlbuMAX that retained the rich composition of RPMI/B27 but was adapted to the physiological needs of CMs. The changes (Figures S1A and S1B) included increased [Ca^{2+}] to a level suited to CM contractility; lower [glucose] to promote FAO; and supplementation with creatine, L-carnitine, and taurine to support CM energetics as used in culture of adult CMs (Schaffer et al., 2010; Volz et al., 1991).

Physiological Phenotyping of hiPSC-CMs Cultured in MM

hiPSC-CMs were differentiated using an established Wnt activator/Wnt inhibitor protocol (see STAR Methods), and at day 20 the cultures were randomized into RPMI/B27 and maturation media (MM) conditions for 3–5 weeks with media changes every 4 days (Figure 1A). Within 24 h of plating in MM, the glucose levels declined sharply from the initial 3 mM to undetectable levels, meaning that the hiPSC-CMs relied on oxidative substrates for most of the time between media changes. By contrast, glucose depletion in RPMI/B27 occurred only after 4 days (Figure S1D). Beat rates were unaffected by decreasing glucose levels in either culture condition, although beat rate was lower in MM than in RPMI/B27 hiPSC-CMs (Figure S1E). The proliferation rate of the hiPSC-CMs declined as measured by 5-ethynyl-2′-deoxyuridine (EdU) incorporation and flow cytometry, decreasing from 12.4% ± 2.7% in RPMI/B27 down to 5.3% ± 1.1% in MM (Figure S2A). An enrichment for CMs also occurred (from 88% ± 2.1% [RPMI/B27] to 95% ± 1.8% [MM]; Figure S2B) as expected because non-CMs in the cultures die without glycolytic substrates (Tohyama et al., 2013). The gain in purity was accompanied by a higher cardiac troponin T (cTnT) mean fluorescent intensity mirrored by increased immunoreactivity and myofibrillar organization of cTnT and α-actinin (Figure S2C).

Immature hiPSC-CMs often rely on Ca^{2+} as the carrier for inward currents to produce electrical responses, whereas Na^+ is used to generate the AP in adult CMs (Sheng et al., 2012). We probed the functionality of Na^+ channels in the two culture conditions using the selective Na^+ channel blocker tetrodotoxin (TTX). TTX induced clear and consistent asystole (cessation of beating) in MM-cultured hiPSC-CMs at a half-maximal inhibitory concentration (IC_{50}) dose (~3.88 μM) consistent with that of the major cardiac Na^+ channel $Na_v1.5$ (Figure 1B). RPMI/B27 hiPSC-CMs were resistant to even the highest TTX concentration (100 μM). Next, we used this as an assay to test whether the media modifications individually would confer TTX sensitivity. No individual modification was sufficient (Figure S1C; note the continued spontaneous firing of APs in the presence of 100 μM TTX), consistent with a synergistic effect on maturation.

We compared the metabolic status of hiPSC-CMs cultured under MM relative to conventional RPMI/B27 culture conditions. hiPSC-CMs maintained in MM showed a higher fatty acid uptake capacity (Figure S1F). hiPSC-CMs cultured in MM had ~30% higher spare and maximal respiration rates than cells maintained for the same time in the standard RPMI/B27 media, as quantified by oxygen consumption rates (OCRs) using the Seahorse analyzer (spare: OCR, MM 172 ± 9 versus RPMI 123 ± 15 pmol/min/cell number; maximal: OCR, MM 202 ± 9 versus RPMI 147 ± 16 pmol/min/cell number), demonstrating enhanced aerobic respiration and ATP production (Figure 1B) across two separate iPSC lines (Figure S2D). The extracellular acidification rate (ECAR) was used to assess glycolytic parameters (Figure 1C), and MM enhanced ECAR by ~40% (ECAR, MM 12.3 ± 2.3 versus RPMI 6.3 ± 1.2 mpH/min/cell number). ECAR in both cultures rose after blocking of ATP synthase with oligomycin, which is used to measure "glycolytic capacity" (ECAR, 17.4 ± 1.7 versus 10.2 ± 0.1 mpH/min/cell number), indicating that hiPSC-CMs in MM can switch between oxidative phosphorylation and glycolysis. This conclusion was corroborated by the maintenance of beat rate through successive cycles of glucose and oxidative substrates (Figures S1B and S1D). These results showed that MM enhanced both oxidative and glycolytic metabolism.

Mitochondrial content and distribution were examined using the mitochondrial marker Tom20. Higher levels of Tom20 immunoreactivity by flow cytometry indicated that the mitochondrial content had increased in MM- relative to RPMI/B27-cultured hiPSC-CMs (Figure 1E). Tom20 immunostaining localized alongside the sarcomere in a punctated pattern (Figure 1F). By contrast, mitochondria in RPMI/B27-cultured hiPSC-CMs were

CellPress
OPEN ACCESS

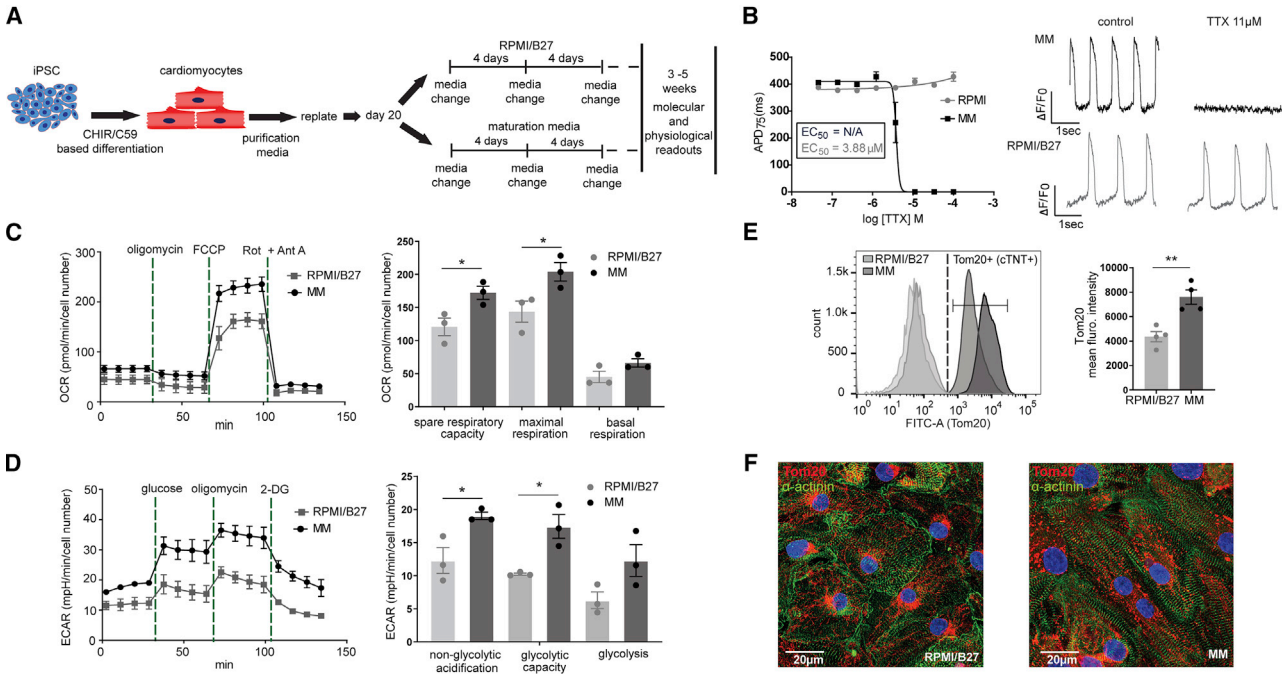

Figure 1. Influence of MM on Metabolism of iPSC-CMs

(A) Schematic overview of the study. Twenty days after the start of differentiation, hiPSC-CMs were separated into maturation media (MM) or standard RPMI/B27 conditions.

(B) Optical AP recordings (VF2.1.Cl dye) revealed functional sodium (Na^+) channels in MM CMs, with cessation of beating occurring at IC_{50} ~3.88 μM. Representative optical voltage recording of control (ctr) and 11 μM TTX-treated MM and RPMI/B27 cells.

(C) Real-time oxygen consumption rate (OCR) measurements of hiPSC-CMs cultured in RPMI/B27 or MM by Seahorse extracellular flux analyzer. Cells were treated with the ATP synthase inhibitor oligomycin, the respiratory uncoupler FCCP, and the respiratory chain blockers rotenone and antimycin A. MM exhibited greater respiration rate under basal conditions and after mitochondrial uncoupling (n = 3 batches).

(D) Real-time ECAR measurements of hiPSC-CMs cultured in RPMI/B27 or MM by Seahorse extracellular flux analyzer. Cells were treated with glucose, ATP synthase inhibitor oligomycin, and glucose analog 2-DG. Maturation conditions induced the glycolytic capacity of cells (n = 3 batches).

(E) Flow cytometry analysis of Tom20 expression in RPMI/27- and MM-cultured hiPSC-CMs revealed higher mitochondrial content in maturation culture (n = 4 batches).

(F) Representative mitochondria (Tom20) immunostaining in hiPSC-CMs cultured in RPMI/B27 and MM. Pronounced differences were observed in Tom20 distribution between the two culture conditions. Scale bars represent 20 μm.

Data are presented as mean ± SEM. *p < 0.05, **p < 0.005, and ***p < 0.0005.

densely packed around the nucleus. Sarcomere-arrayed mitochondria correlate with maturation *in vivo* (Piquereau and Ventura-Clapier, 2018).

MM Activates Metabolic and Cardiac Physiology Gene Expression

The phenotyping data above showed that MM can direct metabolic as well as structural and physiological maturation of hiPSC-CMs. RNA sequencing (RNA-seq) was performed to gain insight into the underlying molecular basis for the changes. Compared with baseline (day 21) conditions, 3 weeks of subsequent exposure to MM and RPMI/B27 (day 41) caused the significant differential expression of 1,308 and 368 genes, respectively ($|\log_2$ fold change$| > \log_2(2)$, $q < 0.05$; Figure 2A; Figures S3A–S3C). There were 862 genes differentially expressed between RPMI/B27 and MM conditions at day 41. Gene Ontology (GO) analysis of the MM differentially upregulated genes was informative, mapping to mitochondrial metabolism (Figure 2B). Individual gene changes (Figure 2C) reflected increased FAO observed by the Seahorse analysis (Figures 1B and 1C) and further supported by upregulation of genes involved in cristae formation and stability (Figure S3C) as well as regulators of mitochondrial Ca^{2+} uptake (Figure S3D). Accordingly, GO analysis of the upregulated transcriptional regulators in MM mapped to energy metabolism and lipid homeostasis (Figures S3F and S3G). Interestingly, multiple Ca^{2+} cycling/SR, sarcomeric, and ion channel genes were differentially expressed (Figures 2D–2F). These gene expression changes indicated that supplementation with oxidative substrates might affect CM electrophysiology, Ca^{2+} cycling, and contractility.

MM Improves Electrophysiological Characteristics

The RNA-seq data (Figure 2F) showed the prominent upregulation of *KCNJ2*, which encodes the pore-forming subunit of the channel that conducts the K^+ current I_{K1} that sets the CM diastolic membrane potential. The characteristically negligible I_{K1} in hiPSC-CMs contributes to aspects of electrophysiological immaturity, including relatively depolarized diastolic potentials

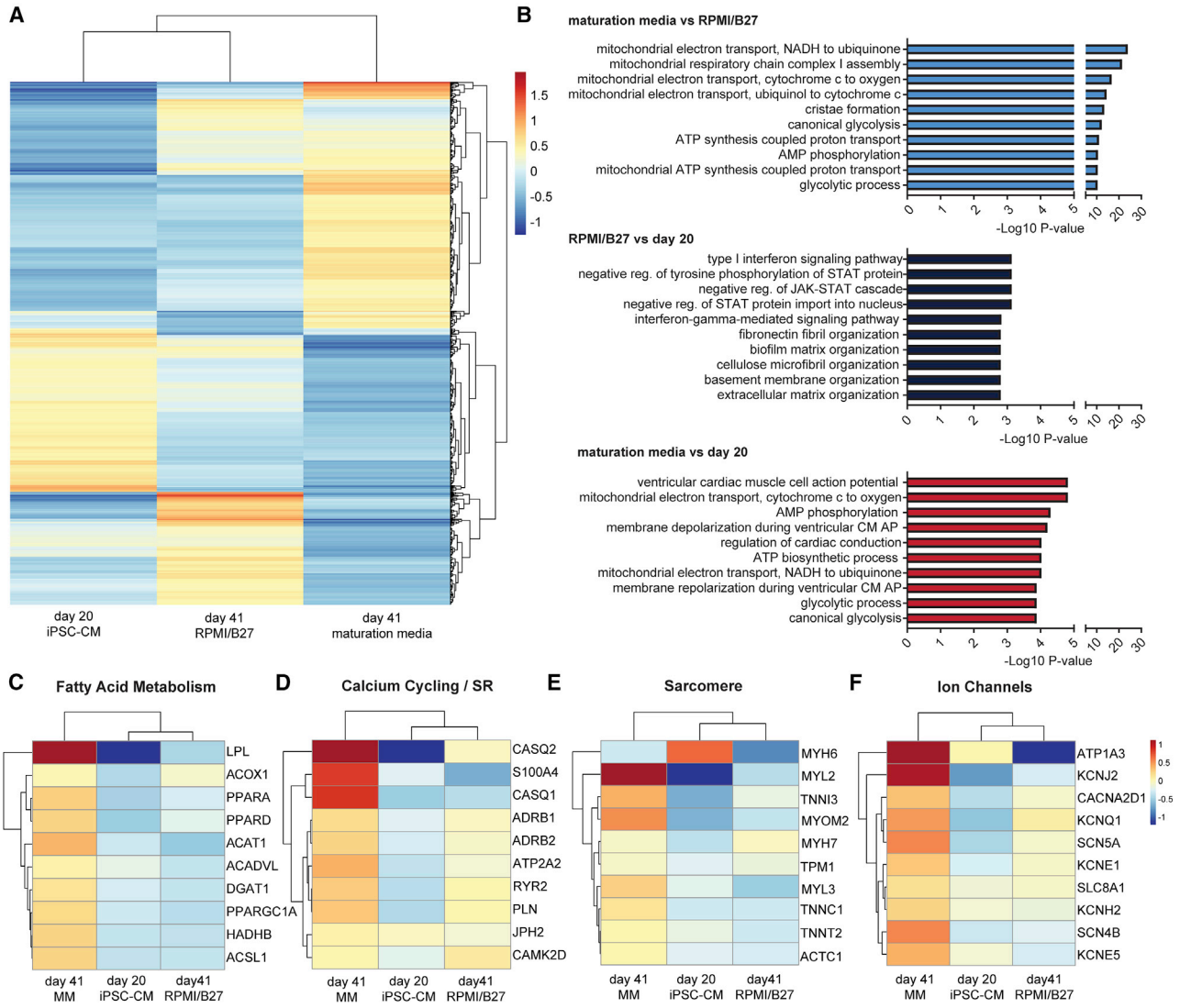

Figure 2. Metabolism and CM Genes Are Upregulated in MM-Treated iPSC-CMs

(A) Heatmap of the top 1,000 genes with highest variance across the three treatment groups.

(B) Top 10 GO terms associated with the differentially expressed genes in the comparison MM versus prolonged RPMI/B27 (top), RPMI/B27 versus baseline differentiation (middle), and MM and baseline differentiation (bottom). The top GO terms associated with maturation are related to metabolism and CM biology.

(C–F) Heatmaps of key genes involved in distinct features of CM behavior: (C) fatty acid metabolism, (D) calcium (Ca^{2+}) cycling and sarcoplasmic reticulum (SR), (E) sarcomere, and (F) ion channels.

RNA-seq experiment was performed on n = 3 iPSC-CM batches.

and low availability of Na^+ channels (Goversen et al., 2018; Horváth et al., 2018; Meijer van Putten et al., 2015). Patch-clamp electrophysiology revealed I_{K1} density to be quite substantial in MM hiPSC-CMs (−10.3 ± 1.2 pA/pF at −140 mV and 1.2 ± 0.2 pA/pF at +60 mV; Figure 3A). These levels are comparable with I_{K1} measured in adult human and rabbit ventricular myocytes (Horváth et al., 2018; Jost et al., 2013; Pogwizd et al., 2001) and much higher than that recorded in RPMI iPSC-CMs (Figure S4A). I_{K1} density was independent of cell capacitance (Figure S4B), indicating that higher I_{K1} function is an intrinsic feature of hiPSC-CMs cultured in MM and not a function of cell size. Consistent with substantial I_{K1}, MM hiPSC-CMs exhibited low spontaneous beating frequency, a polarized diastolic membrane potential of −80.3 ± 0.6 mV (measured with 1 Hz pacing just before the stimulated AP), and a rapid AP upstroke velocity (dV/dt_{max} of 250 ± 18 V/s) (Figure 3B; Figure S4C). The diastolic potential and upstroke velocity values exceeded typical values for pluripotent stem cell-derived CMs and iPSC-CMs in RPMI (Figure S4D) and approached those in normal adult ventricular myocytes, which are typically near −85 mV and ~200–300 V/s, respectively (Chen et al., 2009). We conclude that MM induced maturational effects in cellular electrophysiology, including more I_{K1}, more negative diastolic membrane potential (E_m), and increased reliance on

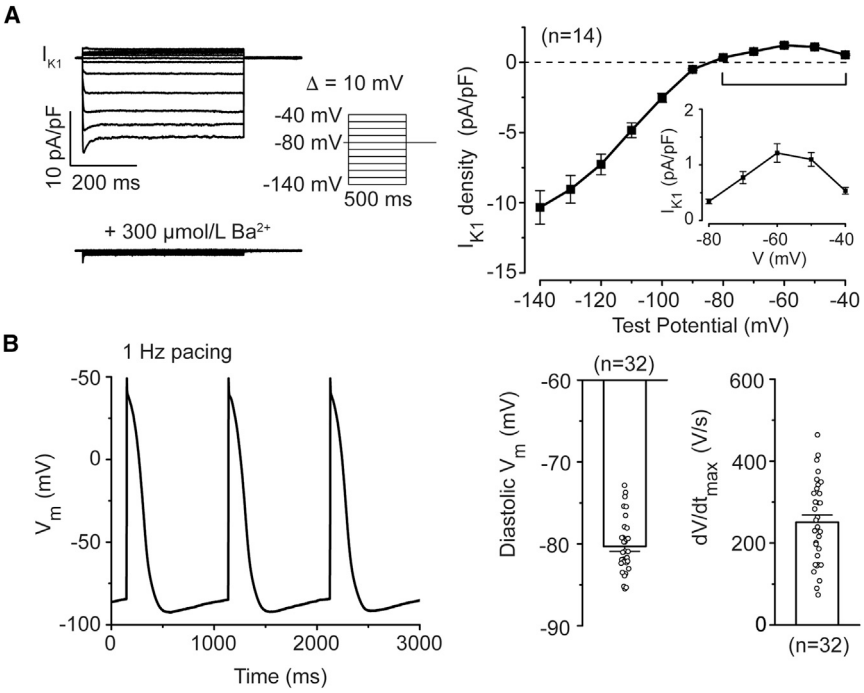

Figure 3. MM Increases I_{K1}, Diastolic Membrane Potential, and Upstroke Velocity of the AP

(A) Large inward rectifier K^+ current (I_{K1}) in single hiPSC-CMs cultured in MM. Representative I_{K1} traces in ctr and following inhibition with 300 μmol/L Ba^{2+}. Outward component of Ba^{2+}-sensitive I_{K1} and voltage protocol are given in insets.

(B) Stimulated APs show highly negative resting membrane potential just prior to the AP (diastolic V_m) and markedly increased AP upstroke velocity (dV/dt_{max}). Patch-clamp recordings were obtained in single hiPSC-CM cultured in MM and paced at 1 Hz frequency.

Data are presented as mean ± SEM.

the Na^+ channel for the cardiac AP upstroke as implied by the increased sensitivity to TTX in Figure 1B.

MM Enhances Ca^{2+} Cycling and Contractility

Efficient Ca^{2+} cycling is critical for CM contraction and relaxation. As CMs mature, a greater proportion of Ca^{2+} cycling involves the SR as opposed to flux across the plasma membrane. MM culture significantly increased expression of proteins encoding the SR Ca^{2+} pump sarco/endoplasmic reticulum Ca^{2+}-ATPase (SERCA2a), its regulator (phospholamban [PLN]), and the main contributor of Ca^{2+} storage inside the SR (calsequestrin 2 [CASQ2]) as well as elevated protein levels of a key player in SR Ca^{2+} release (junctophilin 2 [JPH2]) (Figure 4A). High CASQ2 expression was observed in MM-cultured hiPSC-CMs along the sarcomere, and this expression was absent under RPMI/B27 conditions (Figure S5A). To test the responsiveness of the hiPSC-CMs to sympathetic nervous system regulation, isoproterenol stimulation had a 3-fold higher effect on PLN phosphorylation in MM conditions than in RPMI/B27, indicative of more effective and robust β-adrenergic responsiveness (Figure S5B).

To probe SR function directly, we treated hiPSC-CMs with the selective SERCA2a inhibitor thapsigargin, revealing a greater effect in MM-cultured than RPMI/B27-cultured hiPSC-CMs as quantified by the ~2-fold greater decrease in the slope of the decay phase of the Ca^{2+} transient duration (CTD_{75-25}) (Figure 4B). The increased SR Ca^{2+} dependence was further confirmed by the greater effect of small interfering RNA (siRNA) knockdown of SERCA2a and PLN in two healthy donor (HD) lines (Figure 4C; Figure S5C). To quantify Ca^{2+} dynamics, we measured fura-2 fluorescence under the different culture conditions (Figure 4D). MM markedly enhanced Ca^{2+} decay kinetics in MM cells (tau [s], RPMI 0.87 ± 0.03 versus MM 0.53 ± 0.02 s) consistent with increased SERCA2a activity (Figure 4E; Figure S5D). Furthermore, under electrical pacing conditions, we also observed a lower transient amplitude (0.75 ± 0.03 in RPMI versus 0.54 ± 0.03 in MM) and lower diastolic intracellular Ca^{2+} concentration ($[Ca^{2+}]_i$) (RPMI 1.27 ± 0.02 versus MM 1.09 ± 0.01 paced/non-paced $[Ca^{2+}]$ diastolic ratio) in MM than RPMI/B27 (Figure 4E). These findings can be attributed to the relatively greater capability of the SR to regulate Ca^{2+} fluxes under continuous pacing. Accordingly, more Ca^{2+} was released from the SR upon treatment with caffeine in MM-cultured CMs, indicating greater SR loading (SR load/amplitude, 2.3 ± 0.1 versus 1.4 ± 0.05 in RPMI). Corroborating this finding, the Ca^{2+} transients of most MM-cultured hiPSC-CMs became entrained to high-frequency (2 Hz) field stimulations, whereas none of the tested RPMI/B27-CMs could do so (Figure S5E).

Next, we evaluated whether the enhanced Ca^{2+} cycling translated into increased force generation. Dynamic monolayer force microscopy (DMFM) is a common method to evaluate contractile performance (Figure 4F). hiPSC-CMs were plated on soft polyacrylamide gels of predetermined stiffness (Young's modulus [*E*] = ~8.73 kPa) embedded with fluorescent beads. Bead displacement caused by CM contraction was tracked and used to calculate traction and intracellular stresses (Figures 4F and 4G). Under MM conditions, intracellular tension was significantly increased from 2.01 ± 0.9 to 6.64 ± 2.1 nN/μm, with no changes in contraction frequency (peak-to-peak time). Furthermore, the increase in force was accompanied by increased maximal contraction (RPMI 0.07 ± 0.05 versus MM 0.17 ± 0.06 nN/(μm s)) and relaxation (RPMI 0.04 ± 0.01 versus MM 0.14 ± 0.04 nN/(μm s)) rates as well as faster relaxation (fall) (RPMI 0.21 ± 0.03 versus MM 0.15 ± 0.02 s) times.

MM Enhanced Visualization of Contractile Deficits in an hiPSC-CM Model of DCM

RBM20 is an important RNA splicing regulator in the myocardium that removes introns and reorganizes precursor mRNA (pre-mRNA) coding regions for the expression of alternate protein isoforms in response to developmental and physiological cues (Maatz et al., 2014). RBM20 mutations cause early-onset

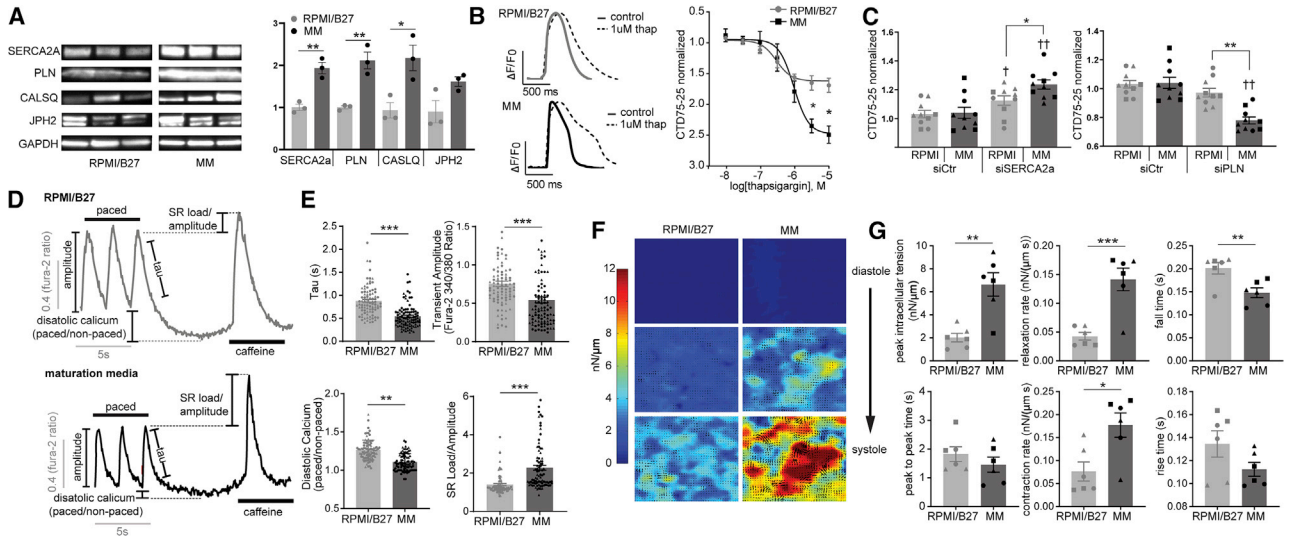

Figure 4. Improved Ca^{2+} Handling Properties of iPSC-CMs in MM

(A) Western blot of SR proteins. SR proteins were markedly increased under maturation conditions (n = 3 batches). SERCA2a, sarco/endoplasmic reticulum Ca^{2+}-ATPase; CASQ, calsequestrin; JPH2, junctophilin 2; PLN, phospholamban.

(B) Representative Fluo-4 traces under both culture conditions either untreated (ctr) or treated with 1 μM thapsigargin (thap). Each trace is an average normalized $\Delta F/F_0$ versus time plot (33 Hz) from multiple peaks in each well (n = 3 peaks). Thapsigargin dose response on hiPSC-CMs highlights the enhanced thapsigargin sensitivity on Ca^{2+} transient duration (CTD) of MM cultured cells (n = 3 batches, n = 3 wells each).

(C) siRNA experiment targeting SERCA2a or PLN in hiPSC-CMs. Optical Fluo-4 recordings showed that MM-cultured cells significantly increased CTD after siSERCA2a compared with siControl (siCtr) and RPMI/B27. Conversely, a significantly lowered CTD was recorded in MM after addition of siPLN (n = 3 batches, n = 3 wells each).

(D) Representative fura-2 Ca^{2+} traces. The changes in intracellular Ca^{2+} concentrations were measured by ratiometric fura-2 indicator. hiPSC-CMs were paced at 0.5 Hz and exposed to caffeine to measure SR Ca^{2+} content.

(E) Quantification of fura-2 recordings. Under pacing conditions, we observed lowered tau, amplitude, and diastolic Ca^{2+} levels in MM cells. After addition of caffeine, MM cells exhibited greater release of SR Ca^{2+} in respect to amplitude (2 batches, n = 39–48 cells each).

(F) Traction force microscopy was performed to assess the effect of the culture media on force generation of cells. Comparison of traction stresses (arrows) and intracellular stresses (heatmap) between MM and RPMI/B27 hiPSC-CMs during a contraction cycle.

(G) Significantly higher traction stresses were observed in MM culture conditions, with no significant changes to the beat rate (peak-to-peak time). Faster contraction kinetics (contraction and relaxation rate) were established in MM conditions (3 batches, n = 2 wells each).

Data are presented as mean ± SEM. Circles (●), squares (■), and triangles (▲) represent experimental batches. For thapsigargin dose-response curve (B), significance was calculated for each dose. For siRNA experiment (C), significance was either calculated compared with respective siControl (†) or with RPMI/B27 conditions (*). † and *$p < 0.05$, †† and **$p < 0.005$, ††† and ***$p < 0.0005$.

DCM due to effects on many proteins, including the sarcomeric protein Titin (TTN), the SR Ca^{2+} channel ryanodine receptor 2 (RyR2), and excitation-contraction coupling kinase Ca^{2+}/calmodulin-dependent protein kinase 2δ. In this respect, RBM20 mutant DCM is well suited to test the effect of MM on the fidelity of disease modeling (Figure 5A). We used CRISPR-Cas9 to insert the RS domain mutation R634Q (Li et al., 2010) into an HD hiPSC line and tested hiPSC-CMs from the isogenic pair (homozygous *RBM20*-WT [wild type] and homozygous *RBM20*-R634Q) under RPMI/B27 and MM conditions. Both culture conditions exhibited defective splicing, visualized as the inclusion of a 24 bp insertion (George et al., 2007) (Figure 5B) as well as the increased expression of the TTN fetal isoform (Maatz et al., 2014) in hiPSC-CMs harboring R634Q mutation (Figure 5C). Impaired cardiac contractility is a hallmark of RBM20 DCM (Li et al., 2010). However, under RPMI/B27 conditions, despite the clear molecular signature of the disease, the hiPSC-CMs did not show contractile dysfunction. By contrast, a contractile deficit of nearly 50% total amplitude was apparent under MM culture conditions (Figure 5D) (amplitude of peak contractile divergence; WT 0.036 ± 0.003 versus R634Q 0.018 ± 0.001).

Phenotypic Manifestation of LQT under MM Conditions

LQT3 is caused by gain-of-function mutations in SCN5A, which encodes the α subunit of the major cardiac Na^+ channel (Bankston et al., 2007). The mutation impairs channel inactivation and causes a persistent late current (I_{NaL}) that prolongs the AP and the QT interval on the surface electrocardiogram (Figures 5E and 5F). MM enhanced Na^+ channel dependence of the AP in hiPSC-CMs (Figure 1B), increased sensitivity to ATX-II (Figure S6A) and the expression of adult-*SCN5a* isoform (Veerman et al., 2017) (Figure S6B), and elevated the maximal Na^+ conductance (G_{max}) (Figure S6H). Hence, we reasoned that it might facilitate modeling of this disorder. To test this idea, we treated LQT3 hiPSC-CMs carrying a disease-causing *SCN5A* F1473C mutation (Terrenoire et al., 2013) with the I_{NaL} blocker mexiletine and compared it with hiPSC-CMs derived from three HD lines. At baseline, LQT3 hiPSC-CMs grown in MM had a significantly increased AP duration compared with both RPMI/B27-grown

CellPress
OPEN ACCESS

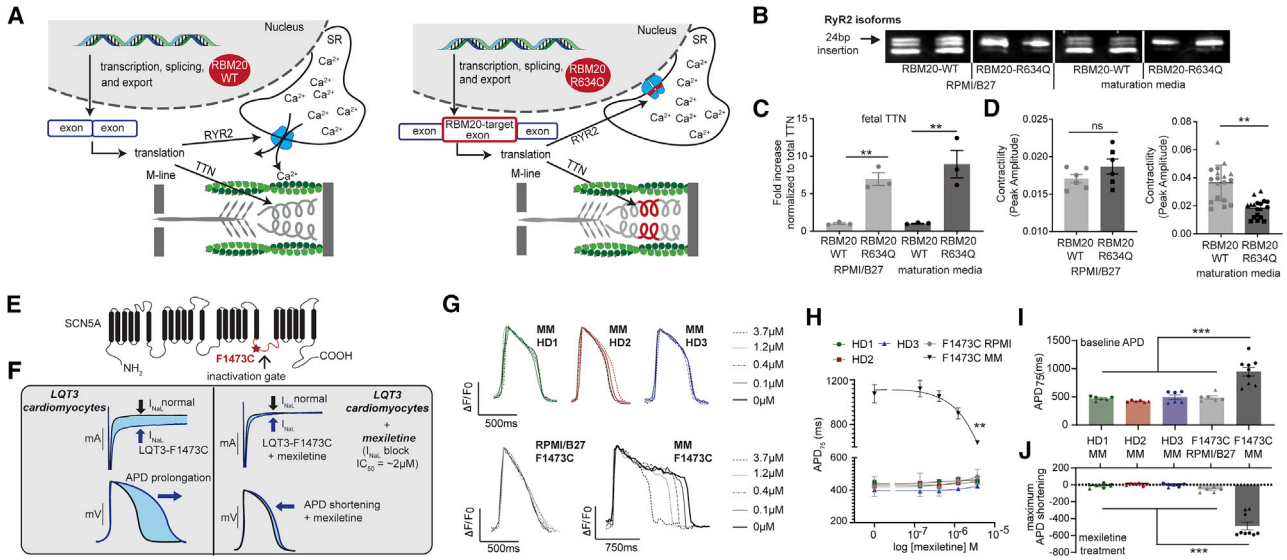

Figure 5. Matured CMs Showed Improved Ability to Recapitulate Contractile and Electrophysiological Dysfunction of DCM and LQT Mutations

(A) Schematic overview highlighting the implication of splicing defect caused by RBM20-R634Q in dilated cardiomyopathy (DCM). Two known mis-spliced targets of RBM20-R6434Q are sarcomeric protein Titin (TTN) and Ca^{2+} regulator ryanodine receptor 2 (RyR2).

(B) Detection of RyR2 isoform expression in RBM20-WT and mutant cell lines under both culture conditions with PCR products on agarose gel. RBM20-R634Q exclusively expressed RyR2 isoform containing 24 bp insert, while RBM20-WT cells also expressed RyR2 without the insert.

(C) qRT-PCR performed on MM and RPMI/B27 samples to establish expression levels of different TTN isoforms in WT or R634Q iPSC-CMs. Significant increased level of fetal TTN was observed in R634Q mutant line with no differences between culture conditions (n = 3 batches).

(D) Contractility performance (KIC, contractility assay) of R634Q iPSC-CMs was significantly impacted by maturation conditions. No significant differences were established in RPMI/B27 media R634Q, but mutation led to profound changes in physiology in MM (RPMI 2 batches, n = 3 wells each; MM 3 batches, n = 6 wells each).

(E) The *SCN5A* F1473C mutation causes congenital long QT syndrome variant 3 (LQT3) by perturbation of channel inactivation.

(F) Schematic overview on the effect of mexiletine. Mexiletine blocks the voltage-gated Na^+ channel to reduce the late Na^+ current (I_{NaL}) and shorten action potential duration (APD) in LQT3 CMs.

(G) Optical recordings with voltage-sensitive dye VF2.1Cl on MM healthy donor (HD) or F1473C hiPSC-CMs grown in either RPMI/B27 or MM. Each trace is an average normalized $\Delta F/F_0$ versus time plot (33 Hz) from multiple peaks in each well (n = 3–5 peaks).

(H) Dose-effect plots of mexiletine on APD (APD_{75}). No APD modulation was noticed in MM-grown HD lines or RPMI/B27-F1473C hiPSC-CMs across mexiletine dose range. A clear dose-dependent APD shortening was observed for MM-F1473C hiPSC-CMs.

(I) Quantification of baseline (no drug treatment) APD (APD_{75}) of individual iPSC-CM lines. MM F1473C hiPSC-CMs exhibited a significantly prolonged APD compared with HD and RPMI/B27-F1473C hiPSC-CMs (2 batches, n = 3–6 wells each).

(J) The effect of mexiletine on iPSC-CMs as shown by the dose with the maximum APD_{75} shortening effect in each culture condition. APD_{75} shortening times (ms) are represented as change from their respective ctr wells. Mexiletine significantly shortened APD in MM *F1473C* compared with HD and RPMI/B27-F1473C hiPSC-CMs (2 batches, n = 3–6 wells each).

Data are presented as mean ± SEM. For mexiletine dose-response curve (H), significance was calculated as change from respective untreated ctr. Circles (●), squares (■), and triangles (▲) represent experimental batches. *p < 0.05, **p < 0.005, and ***p < 0.0005.

LQT3 hiPSC-CMs and the three MM-grown HD lines (Figures 5G and 5I). Furthermore, the MM LQT3 *SCN5A* F1473C hiPSC-CMs responded to treatment with mexiletine with appropriate dose-dependent shortening of the AP ($IC_{50} \sim 0.5$ μM; Figure 5H). By contrast, no shortening was observed in the LQT3 hiPSC-CMs cultured identically in RPMI/B27 (Figure 5J). Interestingly, mexiletine caused no AP shortening in HD hiPSC-CMs in MM, consistent with the effect of the gain-of-function LQT3 mutation.

MM Improves EHT Culture

EHTs are important tools for modeling myocardial function that have potential drug testing utility (Eder et al., 2016). We formed the tissues under the conventional EHT serum-containing media base (control media). When synchronous contraction was observed (between 9 and 14 days), they were randomized to MM and control media groups for an additional 29–42 days. EHTs in MM showed less lactate production relative to glucose consumption (Figures S7A and S7B), indicating increased oxidative metabolism, as well as significantly more mitochondrial content (Figure S7C). EHTs in MM showed a notable difference in the overall tissue morphology: over time EHTs in MM retained their width and vitality completely, whereas in control media they became thinner at the end of the culture period and, in some cases, ruptured or peeled away from their silicone posts (Figures 6A and 6B). Force generation in the viable MM EHTs was increased at the end of the culture period (Figure 6C; Figures S7D and S7E), while spontaneous beat rate was significantly lower in MM culture (beating stopped in some cases after 50 days, while EHTs remained responsive to electrical stimulation). Interestingly, under paced conditions, time to peak was slightly but significantly longer

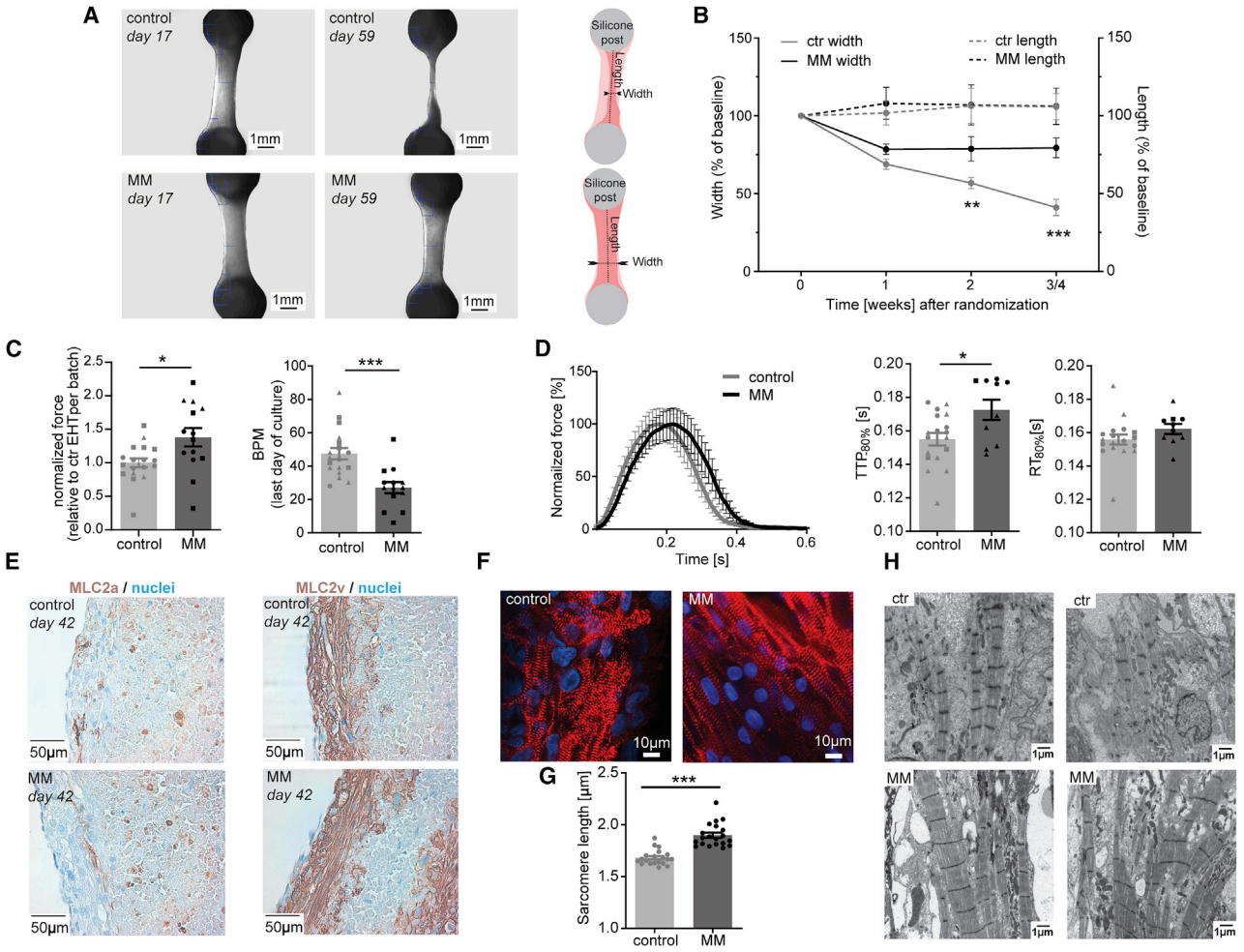

Figure 6. MM Improves the Stability and Functional and Structural Properties of EHTs

(A) Representative images of EHTs prior to switching media (day 17) and after 6 weeks of culture (day 59) in ctr or MM, and schematic overview of the metrics used to quantify EHT integrity and morphology.

(B) Impact of culture conditions on EHT width (plotted on left y axis) and length (plotted on right y axis, dotted lines). Length and width were normalized to baseline (randomization), depicting significantly less thinning of EHTs cultured in MM (n = 18–24, 3 batches).

(C) Average contractile force normalized to the mean force of ctr of the respective batch and spontaneous beat rate (BPM) in the respective medium on the last day of culture (n = 14–18, 3 batches).

(D) Average normalized contraction peaks under electrical stimulation in 1.8 mM Ca^{2+} Tyrode's solution. Note higher time to peak (TTP; 80%) in MM, but similar relaxation time (RT; 80%; n = 9, 3 batches).

(E) Representative MLC2a and MLC2v staining in EHT after 30-day culture in MM or ctr media, depicting mostly MLC2v-positive CMs with a clear longitudinal orientation in both groups.

(F) Representative fluorescent images of α-actinin staining in EHT grown in ctr or MM (scale bar corresponds to 10 µm).

(G) Sarcomeric length as determined by α-actinin staining. Longer sarcomeric length was observed in MM conditions (n = 100 sarcomeres, 2 batches).

(H) Representative electron microscopy images from ctr and MM EHT. Ultrastructures in EHT cultured in MM appeared more defined.

Data are presented as mean ± SEM. Circles (●), squares (■), and triangles (▲) represent experimental batches. *p < 0.05, **p < 0.005, ***p < 0.0005.

in MM EHTs (Figure 6D), while relaxation time was similar, suggesting a higher abundance of the slow β-myosin heavy chain (MHC) isoform. Consistent with this hypothesis, higher β-MHC abundance was observed by western blotting in MM than control media (Figures S7G and S7H). Structurally, the ventricular isoform of myosin light chain 2 (MLC2v) staining revealed a clear longitudinal orientation of the CM in both groups (Figure 6E). EHTs in MM showed a tendency for broader cardiac muscle fibers and significantly longer sarcomere length (1.68 ± 0.02 and 1.90 ± 0.025 µm, respectively; Figures 6F and 6G). Electron microscopy revealed an overall better-defined ultrastructure of myofibrils and Z-discs in MM-cultured cells than in control (Figure 6H). Additionally, the control media EHT's structures showed more signs of cell death and dissolution, including vacuoles and vesicles with deposits. Mitochondria in MM EHTs were well located between sarcomeres and showed better defined cristae (data not shown).

DISCUSSION

An unanticipated finding of our study was that the metabolic MM not only enhanced FAO, as seen recently with fatty acid supplementation (Horikoshi et al., 2019; Lin et al., 2017; Yang et al., 2019), but also affected electrophysiological and mechanical indices of maturation. This observation supports the idea that FAO and maturation signaling events might be directly linked. This is consistent with the involvement of two key FAO regulators, *PPARα* (Marionneau et al., 2008) and *KLF15* (Jeyaraj et al., 2012), in the control of voltage-gated K^+ channel expression in isolated murine CMs including *Kcnh2* and *Kcnq1* genes that code for two main repolarizing currents (slow [I_{Ks}] and rapid [I_{Kr}] activating delayed rectifier potassium currents). Voltage-gated K^+ channels are essential for cardiac repolarization (Nerbonne, 2016), and MM increased both *KCNH2* and *KCNQ1* relative to RPMI/B27 (Figure 2F). Furthermore, we also observed a significant increase in *KCNJ2* and the establishment of a robust I_{K1} current density in MM-cultured cells. I_{K1} is critical for the maintenance of a negative diastolic membrane potential that increases Na^+ channel availability. These electrophysiological media adaptions likely underpin the successful modeling of *SCN5A F1472C* LQT3 mutation in iPSC-CMs.

In addition, RNA-seq data revealed that the MM upregulated multiple Z-disc genes (*DES*, *MYOT*, *MYPN*, *MYOZ2*, *MLP*, and *Tcap*) that have been implicated in a Z-disc signaling hub (Knöll et al., 2011; Vafiadaki et al., 2015) responsible for linking mechanical stresses to downstream signaling events (Frank and Frey, 2011). Upregulation of this signaling module might contribute to coordinated sarcomeric organization under MM conditions. It might also contribute to the ability of our media to reveal a contractile deficit in RBM20 R634Q in hiPSC-CMs (Figure 5). Although outside the scope of this paper, studying whether these signaling pathways are perturbed in RBM20 R634Q mutant CMs might shed light on the basis for the deterioration of contractile function in DCM patients with this and other RBM20 RS domain mutations.

Auxotonic contraction against a mechanical load in 3D EHTs is well known to enhance structural, functional, electrophysiological, and metabolic maturation relative to monolayer cultures (Horváth et al., 2018; Mannhardt et al., 2016; Ulmer et al., 2018). This included more mitochondria and a preference for oxidative metabolism in medium with all energy substrates available. However, the standard culture medium of EHTs with serum and glucose and the absence of fatty acids as energy substrate still resulted in mostly anaerobic glycolysis, leading to lactate production (Figure S7A). MM culture of EHTs in MM led to enhanced maturation, exemplified by better sarcomeric organization, higher abundance of the slow β-MHC isoform, slower contraction, lower beating rate, and higher force development (Figure 5D). In addition, long-term stability of 3D EHTs was enhanced, probably because fibrin degradation enzymes derived from serum were absent.

Although we have not thoroughly examined the contribution of individual media components to the observed physiological effects, recent studies suggest mechanistic insight into the relationship between energy substrates and physiological maturation. Nakano et al. (2017) showed that glucose inhibits maturation of human embryonic stem cell (hESC)-derived CMs through the pentose phosphate pathway. Moreover, chronic hyperglycemic conditions can have detrimental consequences for cultured cells (Sorrentino et al., 2017). On the other hand, chronic glucose starvation in myocytes leads to excessive reactive oxygen species (ROS) production in myocytes (Marambio et al., 2010) and is essential for nucleotide and amino acid syntheses. Thus, the glucose levels in the MM were designed to provide periodic exposure to glucose in order to support physiological processes important for cardiac development, while also driving cells to shift to oxidative metabolism between media exchanges. It will be interesting to determine how the control of glycolysis and the pentose phosphate pathway (and the balance between hyperglycemia and glucose starvation) influences maturation. Another consideration is the B27 supplement, which is complex and has been shown to contain components that negatively affect CM differentiation efficiency (Pei et al., 2017). Whether these or other individual components negatively impact physiological maturation is unclear, and a detailed optimization might enhance maturation beyond that which we have achieved. Lastly, modulators such as triiodothyronine (T3) and/or dexamethasone and miR-1/miR-499 can also enhance electromechanical maturation of iPSC-CMs (Fu et al., 2011; Parikh et al., 2017; Yang et al., 2014b). It is interesting to speculate that metabolic maturation might induce distinct molecular signaling from that caused by hormonal, microRNA, or 3D EHT electromechanical stimulation; therefore, it would be interesting to explore whether these might have additive or synergistic effects in combination with our metabolic maturation protocol.

In summary, we developed media formulation for the physiological maturation of hiPSC-CMs that differs from conventional hiPSC-CM media by providing oxidative substrates, L-carnitine, taurine, and [Ca^{2+}], with low glucose, to support FAO oxidation and physiological function of CMs. A key finding was that hiPSC-CMs maintained in this media enhanced electrophysiological, mechanical, and structural indices of physiological maturation, suggesting that increasing FAO activates signaling that coordinates these non-metabolic aspects of normal developmental maturation. We showed that this media enabled the reproducible and statistically robust modeling of two congenital heart diseases in patient hiPSC-CMs in 384-well monolayer culture suitable for high-throughput screening. In 3D EHTs, the MM enhanced sarcomeric function, reduced statistical variation, and decreased dropout of the cultures over time. Thus, this media can be widely applied to support basic and translational goals using hiPSC-CM cultures.

STAR★METHODS

Detailed methods are provided in the online version of this paper and include the following:

- KEY RESOURCES TABLE
- RESOURCE AVAILABILITY
  - Lead Contact
  - Materials Availability
  - Data and Code Availability

SUPPLEMENTAL INFORMATION

Supplemental Information can be found online at https://doi.org/10.1016/j.celrep.2020.107925.

ACKNOWLEDGMENTS

We gratefully acknowledge the help from Thomas Schulze, Birgit Klampe, Kristin Hartmann, Philine Braun, Jascha Sani, Arne Hansen, and Alex Lee. This research was supported by grants from the NIH (R01HL113006, R01HL130840, R01HL128072, R21HL141019 and R01HL132225 to M.M. and P01HL141084 to M.M. and J.C.W.); Foundation Leducq (CurePLaN) to M.M.; AHA (18CDA34070040) to C.W.; and CIRM (RB5-07356) to C.M.M. D.A.M.F. was funded by the European Union's Horizon 2020 research and innovation programme under the Marie Sklodowska-Curie grant agreement 708459.

AUTHOR CONTRIBUTIONS

Conceptualization, D.A.M.F., W.L.M., A.A.N.B., H.Z., S.S., C.M.M., and M.M.; Methodology, D.A.M.F., W.L.M., A.A.N.B., and M.M.; Investigation, D.A.M.F., W.L.M., A.A.N.B., S.S., L.H., B.U., F.B., M.S., B.H., Z.L., R.-P.P., K.S.G., C.K.L., R.S., C.W., A.K., M.V., P.L.A., C.S.B., S.R., R.G.C.M., and M.G.; Writing – Original Draft, D.A.M.F., W.L.M., A.A.N.B., and M.M.; Writing – Review & Editing, all authors; Funding Acquisition, D.A.M.F., C.W., D.B., J.C.W., D.M.B., T.E., C.M.M., and M.M.; Supervision, J.C.W., D.M.B., T.E., and M.M.

DECLARATION OF INTERESTS

The authors declare no competing interests. A patent application related to this work has been submitted.

Received: March 25, 2020
Revised: May 15, 2020
Accepted: June 26, 2020
Published: July 21, 2020

REFERENCES

Banerjee, I., Carrion, K., Serrano, R., Dyo, J., Sasik, R., Lund, S., Willems, E., Aceves, S., Meili, R., Mercola, M., et al. (2015). Cyclic stretch of embryonic cardiomyocytes increases proliferation, growth, and expression while repressing Tgf-β signaling. J. Mol. Cell. Cardiol. *79*, 133–144.

Bankston, J.R., Yue, M., Chung, W., Spyres, M., Pass, R.H., Silver, E., Sampson, K.J., and Kass, R.S. (2007). A novel and lethal de novo LQT-3 mutation in a newborn with distinct molecular pharmacology and therapeutic response. PLoS ONE *2*, e1258.

Breckwoldt, K., Letuffe-Brenière, D., Mannhardt, I., Schulze, T., Ulmer, B., Werner, T., Benzin, A., Klampe, B., Reinsch, M.C., Laufer, S., et al. (2017). Differentiation of cardiomyocytes and generation of human engineered heart tissue. Nat. Protoc. *12*, 1177–1197.

Bruyneel, A.A.N., McKeithan, W.L., Feyen, D.A.M., and Mercola, M. (2018). Using iPSC Models to Probe Regulation of Cardiac Ion Channel Function. Curr. Cardiol. Rep. *20*, 57.

Cerignoli, F., Charlot, D., Whittaker, R., Ingermanson, R., Gehalot, P., Savchenko, A., Gallacher, D.J., Towart, R., Price, J.H., McDonough, P.M., and Mercola, M. (2012). High throughput measurement of Ca^{2+} dynamics for drug risk assessment in human stem cell-derived cardiomyocytes by kinetic image cytometry. J. Pharmacol. Toxicol. Methods *66*, 246–256.

Chen, H.S., Kim, C., and Mercola, M. (2009). Electrophysiological challenges of cell-based myocardial repair. Circulation *120*, 2496–2508.

Del Alamo, J.C., Meili, R., Alonso-Latorre, B., Rodríguez-Rodríguez, J., Aliseda, A., Firtel, R.A., and Lasheras, J.C. (2007). Spatio-temporal analysis of eukaryotic cell motility by improved force cytometry. Proc. Natl. Acad. Sci. USA *104*, 13343–13348.

Eder, A., Vollert, I., Hansen, A., and Eschenhagen, T. (2016). Human engineered heart tissue as a model system for drug testing. Adv. Drug Deliv. Rev. *96*, 214–224.

Frank, D., and Frey, N. (2011). Cardiac Z-disc signaling network. J. Biol. Chem. *286*, 9897–9904.

Fu, J.D., Rushing, S.N., Lieu, D.K., Chan, C.W., Kong, C.W., Geng, L., Wilson, K.D., Chiamvimonvat, N., Boheler, K.R., Wu, J.C., et al. (2011). Distinct roles of microRNA-1 and -499 in ventricular specification and functional maturation of human embryonic stem cell-derived cardiomyocytes. PLoS ONE *6*, e27417.

Gaspar, J.A., Doss, M.X., Hengstler, J.G., Cadenas, C., Hescheler, J., and Sachinidis, A. (2014). Unique metabolic features of stem cells, cardiomyocytes, and their progenitors. Circ. Res. *114*, 1346–1360.

George, C.H., Rogers, S.A., Bertrand, B.M., Tunwell, R.E., Thomas, N.L., Steele, D.S., Cox, E.V., Pepper, C., Hazeel, C.J., Claycomb, W.C., and Lai, F.A. (2007). Alternative splicing of ryanodine receptors modulates cardiomyocyte Ca2+ signaling and susceptibility to apoptosis. Circ. Res. *100*, 874–883.

Goversen, B., van der Heyden, M.A.G., van Veen, T.A.B., and de Boer, T.P. (2018). The immature electrophysiological phenotype of iPSC-CMs still hampers in vitro drug screening: Special focus on I_{K1}. Pharmacol. Ther. *183*, 127–136.

Greensmith, D.J. (2014). Ca analysis: an Excel based program for the analysis of intracellular calcium transients including multiple, simultaneous regression analysis. Comput. Methods Programs Biomed. *113*, 241–250.

Hansen, A., Eder, A., Bönstrup, M., Flato, M., Mewe, M., Schaaf, S., Aksehirlioglu, B., Schwoerer, A.P., Uebeler, J., and Eschenhagen, T. (2010). Development of a drug screening platform based on engineered heart tissue. Circ. Res. *107*, 35–44.

Hom, J.R., Quintanilla, R.A., Hoffman, D.L., de Mesy Bentley, K.L., Molkentin, J.D., Sheu, S.S., and Porter, G.A., Jr. (2011). The permeability transition pore controls cardiac mitochondrial maturation and myocyte differentiation. Dev. Cell *21*, 469–478.

Horikoshi, Y., Yan, Y., Terashvili, M., Wells, C., Horikoshi, H., Fujita, S., Bosnjak, Z.J., and Bai, X. (2019). Fatty Acid-Treated Induced Pluripotent Stem Cell-Derived Human Cardiomyocytes Exhibit Adult Cardiomyocyte-Like Energy Metabolism Phenotypes. Cells *8*, 1095.

Horváth, A., Lemoine, M.D., Löser, A., Mannhardt, I., Flenner, F., Uzun, A.U., Neuber, C., Breckwoldt, K., Hansen, A., Girdauskas, E., et al. (2018). Low Resting Membrane Potential and Low Inward Rectifier Potassium Currents

Are Not Inherent Features of hiPSC-Derived Cardiomyocytes. Stem Cell Rep. *10*, 822–833.

Jeyaraj, D., Haldar, S.M., Wan, X., McCauley, M.D., Ripperger, J.A., Hu, K., Lu, Y., Eapen, B.L., Sharma, N., Ficker, E., et al. (2012). Circadian rhythms govern cardiac repolarization and arrhythmogenesis. Nature *483*, 96–99.

Jost, N., Virág, L., Comtois, P., Ordög, B., Szuts, V., Seprényi, G., Bitay, M., Kohajda, Z., Koncz, I., Nagy, N., et al. (2013). Ionic mechanisms limiting cardiac repolarization reserve in humans compared to dogs. J. Physiol. *591*, 4189–4206.

Knöll, R., Linke, W.A., Zou, P., Miocic, S., Kostin, S., Buyandelger, B., Ku, C.H., Neef, S., Bug, M., Schäfer, K., et al. (2011). Telethonin deficiency is associated with maladaptation to biomechanical stress in the mammalian heart. Circ. Res. *109*, 758–769.

Kolwicz, S.C., Jr., Purohit, S., and Tian, R. (2013). Cardiac metabolism and its interactions with contraction, growth, and survival of cardiomyocytes. Circ. Res. *113*, 603–616.

Lam, C.K., Zhao, W., Cai, W., Vafiadaki, E., Florea, S.M., Ren, X., Liu, Y., Robbins, N., Zhang, Z., Zhou, X., et al. (2013). Novel role of HAX-1 in ischemic injury protection involvement of heat shock protein 90. Circ. Res. *112*, 79–89.

Lamason, R.L., Bastounis, E., Kafai, N.M., Serrano, R., Del Alamo, J.C., Theriot, J.A., and Welch, M.D. (2016). Rickettsia Sca4 Reduces Vinculin-Mediated Intercellular Tension to Promote Spread. Cell *167*, 670–683.

Li, D., Morales, A., Gonzalez-Quintana, J., Norton, N., Siegfried, J.D., Hofmeyer, M., and Hershberger, R.E. (2010). Identification of novel mutations in RBM20 in patients with dilated cardiomyopathy. Clin. Transl. Sci. *3*, 90–97.

Lian, X., Hsiao, C., Wilson, G., Zhu, K., Hazeltine, L.B., Azarin, S.M., Raval, K.K., Zhang, J., Kamp, T.J., and Palecek, S.P. (2012). Robust cardiomyocyte differentiation from human pluripotent stem cells via temporal modulation of canonical Wnt signaling. Proc. Natl. Acad. Sci. USA *109*, E1848–E1857.

Lin, B., Lin, X., Stachel, M., Wang, E., Luo, Y., Lader, J., Sun, X., Delmar, M., and Bu, L. (2017). Culture in Glucose-Depleted Medium Supplemented with Fatty Acid and 3,3′,5-Triiodo-l-Thyronine Facilitates Purification and Maturation of Human Pluripotent Stem Cell-Derived Cardiomyocytes. Front. Endocrinol. (Lausanne) *8*, 253.

Lloyd, S.G., Wang, P., Zeng, H., and Chatham, J.C. (2004). Impact of low-flow ischemia on substrate oxidation and glycolysis in the isolated perfused rat heart. Am. J. Physiol. Heart Circ. Physiol. *287*, H351–H362.

Maatz, H., Jens, M., Liss, M., Schafer, S., Heinig, M., Kirchner, M., Adami, E., Rintisch, C., Dauksaite, V., Radke, M.H., et al. (2014). RNA-binding protein RBM20 represses splicing to orchestrate cardiac pre-mRNA processing. J. Clin. Invest. *124*, 3419–3430.

Mannhardt, I., Breckwoldt, K., Letuffe-Brenière, D., Schaaf, S., Schulz, H., Neuber, C., Benzin, A., Werner, T., Eder, A., Schulze, T., et al. (2016). Human Engineered Heart Tissue: Analysis of Contractile Force. Stem Cell Rep. *7*, 29–42.

Marambio, P., Toro, B., Sanhueza, C., Troncoso, R., Parra, V., Verdejo, H., García, L., Quiroga, C., Munafo, D., Díaz-Elizondo, J., et al. (2010). Glucose deprivation causes oxidative stress and stimulates aggresome formation and autophagy in cultured cardiac myocytes. Biochim. Biophys. Acta *1802*, 509–518.

Marionneau, C., Aimond, F., Brunet, S., Niwa, N., Finck, B., Kelly, D.P., and Nerbonne, J.M. (2008). PPARalpha-mediated remodeling of repolarizing voltage-gated K+ (Kv) channels in a mouse model of metabolic cardiomyopathy. J. Mol. Cell. Cardiol. *44*, 1002–1015.

McKeithan, W.L., Savchenko, A., Yu, M.S., Cerignoli, F., Bruyneel, A.A.N., Price, J.H., Colas, A.R., Miller, E.W., Cashman, J.R., and Mercola, M. (2017). An Automated Platform for Assessment of Congenital and Drug-Induced Arrhythmia with hiPSC-Derived Cardiomyocytes. Front. Physiol. *8*, 766.

Meijer van Putten, R.M., Mengarelli, I., Guan, K., Zegers, J.G., van Ginneken, A.C., Verkerk, A.O., and Wilders, R. (2015). Ion channelopathies in human induced pluripotent stem cell derived cardiomyocytes: a dynamic clamp study with virtual IK1. Front. Physiol. *6*, 7.

Nakano, H., Minami, I., Braas, D., Pappoe, H., Wu, X., Sagadevan, A., Vergnes, L., Fu, K., Morselli, M., Dunham, C., et al. (2017). Glucose inhibits cardiac muscle maturation through nucleotide biosynthesis. eLife *6*, e29330.

Nerbonne, J.M. (2016). Molecular Basis of Functional Myocardial Potassium Channel Diversity. Card. Electrophysiol. Clin. *8*, 257–273.

Parikh, S.S., Blackwell, D.J., Gomez-Hurtado, N., Frisk, M., Wang, L., Kim, K., Dahl, C.P., Fiane, A., Tønnessen, T., Kryshtal, D.O., et al. (2017). Thyroid and Glucocorticoid Hormones Promote Functional T-Tubule Development in Human-Induced Pluripotent Stem Cell-Derived Cardiomyocytes. Circ. Res. *121*, 1323–1330.

Pei, F., Jiang, J., Bai, S., Cao, H., Tian, L., Zhao, Y., Yang, C., Dong, H., and Ma, Y. (2017). Chemical-defined and albumin-free generation of human atrial and ventricular myocytes from human pluripotent stem cells. Stem Cell Res. (Amst.) *19*, 94–103.

Piquereau, J., and Ventura-Clapier, R. (2018). Maturation of Cardiac Energy Metabolism During Perinatal Development. Front. Physiol. *9*, 959.

Pogwizd, S.M., Schlotthauer, K., Li, L., Yuan, W., and Bers, D.M. (2001). Arrhythmogenesis and contractile dysfunction in heart failure: Roles of sodium-calcium exchange, inward rectifier potassium current, and residual beta-adrenergic responsiveness. Circ. Res. *88*, 1159–1167.

Pohlmann, L., Kröger, I., Vignier, N., Schlossarek, S., Krämer, E., Coirault, C., Sultan, K.R., El-Armouche, A., Winegrad, S., Eschenhagen, T., and Carrier, L. (2007). Cardiac myosin-binding protein C is required for complete relaxation in intact myocytes. Circ. Res. *101*, 928–938.

Ran, F.A., Hsu, P.D., Wright, J., Agarwala, V., Scott, D.A., and Zhang, F. (2013). Genome engineering using the CRISPR-Cas9 system. Nat. Protoc. *8*, 2281–2308.

Saggerson, D. (2008). Malonyl-CoA, a key signaling molecule in mammalian cells. Annu. Rev. Nutr. *28*, 253–272.

Schaffer, S.W., Jong, C.J., Ramila, K.C., and Azuma, J. (2010). Physiological roles of taurine in heart and muscle. J. Biomed. Sci. *17* (*Suppl 1*), S2.

Serrano, R., Aung, A., Yeh, Y.T., Varghese, S., Lasheras, J.C., and Del Álamo, J.C. (2019). Three-Dimensional Monolayer Stress Microscopy. Biophys. J. *117*, 111–128.

Sharma, A., Burridge, P.W., McKeithan, W.L., Serrano, R., Shukla, P., Sayed, N., Churko, J.M., Kitani, T., Wu, H., Holmström, A., et al. (2017). High-throughput screening of tyrosine kinase inhibitor cardiotoxicity with human induced pluripotent stem cells. Sci. Transl. Med. *9*, eaaf2584.

Sheng, X., Reppel, M., Nguemo, F., Mohammad, F.I., Kuzmenkin, A., Hescheler, J., and Pfannkuche, K. (2012). Human pluripotent stem cell-derived cardiomyocytes: response to TTX and lidocain reveals strong cell to cell variability. PLoS ONE *7*, e45963.

Sorrentino, A., Borghetti, G., Zhou, Y., Cannata, A., Meo, M., Signore, S., Anversa, P., Leri, A., Goichberg, P., Qanud, K., et al. (2017). Hyperglycemia induces defective Ca2+ homeostasis in cardiomyocytes. Am. J. Physiol. Heart Circ. Physiol. *312*, H150–H161.

Tambe, D.T., Croutelle, U., Trepat, X., Park, C.Y., Kim, J.H., Millet, E., Butler, J.P., and Fredberg, J.J. (2013). Monolayer stress microscopy: limitations, artifacts, and accuracy of recovered intercellular stresses. PLoS ONE *8*, e55172.

Terrenoire, C., Wang, K., Tung, K.W., Chung, W.K., Pass, R.H., Lu, J.T., Jean, J.C., Omari, A., Sampson, K.J., Kotton, D.N., et al. (2013). Induced pluripotent stem cells used to reveal drug actions in a long QT syndrome family with complex genetics. J. Gen. Physiol. *141*, 61–72.

Tohyama, S., Hattori, F., Sano, M., Hishiki, T., Nagahata, Y., Matsuura, T., Hashimoto, H., Suzuki, T., Yamashita, H., Satoh, Y., et al. (2013). Distinct metabolic flow enables large-scale purification of mouse and human pluripotent stem cell-derived cardiomyocytes. Cell Stem Cell *12*, 127–137.

Ulmer, B.M., Stoehr, A., Schulze, M.L., Patel, S., Gucek, M., Mannhardt, I., Funcke, S., Murphy, E., Eschenhagen, T., and Hansen, A. (2018). Contractile Work Contributes to Maturation of Energy Metabolism in hiPSC-Derived Cardiomyocytes. Stem Cell Rep. *10*, 834–847.

Vafiadaki, E., Arvanitis, D.A., and Sanoudou, D. (2015). Muscle LIM Protein: Master regulator of cardiac and skeletal muscle functions. Gene *566*, 1–7.

van Weeghel, M., Abdurrachim, D., Nederlof, R., Argmann, C.A., Houtkooper, R.H., Hagen, J., Nabben, M., Denis, S., Ciapaite, J., Kolwicz, S.C., Jr., et al. (2018). Increased cardiac fatty acid oxidation in a mouse model with decreased malonyl-CoA sensitivity of CPT1B. Cardiovasc Res. *114*, 1324–1334.

Veerman, C.C., Mengarelli, I., Lodder, E.M., Kosmidis, G., Bellin, M., Zhang, M., Dittmann, S., Guan, K., Wilde, A.A.M., Schulze-Bahr, E., et al. (2017). Switch From Fetal to Adult *SCN5A* Isoform in Human Induced Pluripotent Stem Cell-Derived Cardiomyocytes Unmasks the Cellular Phenotype of a Conduction Disease-Causing Mutation. J. Am. Heart Assoc. *6*, e005135.

Volz, A., Piper, H.M., Siegmund, B., and Schwartz, P. (1991). Longevity of adult ventricular rat heart muscle cells in serum-free primary culture. J. Mol. Cell. Cardiol. *23*, 161–173.

Yang, X., Pabon, L., and Murry, C.E. (2014a). Engineering adolescence: maturation of human pluripotent stem cell-derived cardiomyocytes. Circ. Res. *114*, 511–523.

Yang, X., Rodriguez, M., Pabon, L., Fischer, K.A., Reinecke, H., Regnier, M., Sniadecki, N.J., Ruohola-Baker, H., and Murry, C.E. (2014b). Tri-iodo-l-thyronine promotes the maturation of human cardiomyocytes-derived from induced pluripotent stem cells. J. Mol. Cell. Cardiol. *72*, 296–304.

Yang, X., Rodriguez, M.L., Leonard, A., Sun, L., Fischer, K.A., Wang, Y., Ritterhoff, J., Zhao, L., Kolwicz, S.C., Jr., Pabon, L., et al. (2019). Fatty Acids Enhance the Maturation of Cardiomyocytes Derived from Human Pluripotent Stem Cells. Stem Cell Rep. *13*, 657–668.

Zhang, H., Badur, M.G., Spiering, S., Divakaruni, A., Meurs, N.E., Murphy, A.N., Mercola, M., and Metallo, C.M. (2020). Lipid availability influences the metabolic maturation of human pluripotent stem cell-derived cardiomyocytes. bioRxiv, 101101/20200314991927.

STAR★METHODS

KEY RESOURCES TABLE

REAGENT or RESOURCE	SOURCE	IDENTIFIER
Antibodies		
Rabbit monoclonal anti-Troponin I (IF)	Thermo Fisher	701585; RRID:AB_2532494
Mouse monoclonal anti-Tom20 (FACS/IF)	Santa Cruz	sc17764; RRID:AB_628381
Mouse monoclonal anti-SERCA2 (WB)	Santa Cruz	sc376235; RRID:AB_10989947
Mouse monoclonal anti-PLN (WB)	abcam	AB2865; RRID:AB_2167905
Rabbit polyclonal anti-JPH2 (WB)	Thermo Fisher	40-5300; RRID:AB_2533471
Rabbit monoclonal anti- Troponin T (FACS)	Thermo Fisher	701620; RRID:AB_2532495
Mouse monoclonal anti- α-actinin (IF)	Sigma Aldrich	A7811; RRID:AB_476766
Rabbit polyclonal anti-phospho-PLN (WB)	Cell Signaling	8496S; RRID:AB_10949102
Rabbit polyclonal anti-CASQ (WB/IF)	abcam	AB3516; RRID:AB_303865
Mouse-monoclonal anti-GADPH HRP conjugated (WB)	Thermo Fisher	MA5-15738; RRID:AB_2537659
Mouse monoclonal anti- β-actin (WB)	Santa Cruz	sc-47778; RRID:AB_626632
Rabbit polyclonal anti- α-MHC (WB, EHT)	Theresia Kraft, Hannover	N/A
Mouse monoclonal anti-β-MHC (WB, EHT)	Sigma	M-8421; RRID:AB_477248
Mouse monoclonal anti-cTNT (WB, ETH)	Thermo Fischer	MA5-12960; RRID:AB_11000742
Rabbit polyclonal anti- α-actinin (IF, EHT)	Thermo Fischer	PA5-16891; RRID:AB_10984790
Critical Commercial Assays		
Seahorse XF Cell Mito Stress Kit	Agilent Technologies	103015-100
Seahorse XF Cell Glycolysis Stress Kit	Agilent Technologies	103020-100
Click-iT EdU Alexa Fluor 647	Thermo Fisher	C10424
Glucose assay kit	Abcam	ab65333
Free Fatty Acid Uptake Assay Kit	Abcam	ab176768
miRVana isolation kit	Thermo Fisher	AM1560
iTaq SYBR Green Supermix	Bio-Rad	1725120
Deposited Data		
RNA sequencing dataset	This paper	GSE151279
Experimental Models: Cell Lines		
Human iPSC line (healthy donor 1)	SCVI Biobank	SCVI-273
Human iPSC line (healthy donor 2)	SCVI Biobank	SCVI-15S1
Human iPSC line (healthy donor 3)	SCVI Biobank	SCVI-113
Human iPSC- *RBM20 R634Q*	This paper	N/A
Human iPSC- *SCN5a F1473c*	McKeithan et al., 2017	N/A
Oligonucleotides		
siRNA targeting SERCA2a	Thermo Fisher	s1748
siRNA targeting PLN	Thermo Fisher	s10669
Primer used in this study, see Table S1	This paper	N/A
Recombinant DNA		
pSpCas9(BB)-2A-GFP	Ran et al., 2013	Addgene plasmid # 48138
Software and Algorithms		
Cytseer software	Vala Sciences	http://www.valasciences.com/
Seahorse Wave Software	Agilent Technologies	https://www.agilent.com/en/products/cell-analysis/cell-analysis-software/data-analysis/wave-desktop-2-6
Flowjo	BD biosciences	https://www.flowjo.com/

(*Continued on next page*)

Continued

REAGENT or RESOURCE	SOURCE	IDENTIFIER
GraphPad Prism	GraphPad Software	https://www.graphpad.com/scientific-software/prism/
ImageJ	NIH	https://imagej.nih.gov/ij/
Zeiss Zen software	Zeiss	https://www.zeiss.com/microscopy/us/products/microscope-software/zen-lite.html

RESOURCE AVAILABILITY

Lead Contact

Further information and requests for resources and reagents should be directed to and will be fulfilled by the Lead Contact, Mark Mercola (mmercola@stanford.edu)

Materials Availability

Further information and requests for resources should be directed to and will be fulfilled by the Lead Contact. All unique reagents generated in this study are available from the Lead Contact with a completed Materials Transfer Agreement.

Data and Code Availability

The datasets generated during this study are available at the NCBI Gene Expression Omnibus (GEO) as accession number GEO: GSE151279.

EXPERIMENTAL MODEL AND SUBJECT DETAILS

Human iPSC culture and differentiation

The protocols used in this study were approved by the Stanford University Institutional Review Board. Sendai viral vector was used for the reprogramming human fibroblasts. The obtained hiPSC clones were cultured in E8 cell culture media (Thermo Fisher Scientific, A1517001) in plates coated with growth factor-reduced Matrigel (Corning, 356231) until at least passage 20 before differentiation. Once confluent, the hiPSC cells were differentiated into human CMs utilizing a chemically-defined cardiomyocyte differentiation protocol (Lian et al., 2012). Briefly, hiPSCs were treated with CHIR99021 (Tocris, 4423) for 3 days in RPMI 1640 (Thermo Fisher Scientific, 11875119) with B27-insulin (Thermo Fisher Scientific, A1895601). Subsequently the cells were treated with the Wnt inhibitor C59 (Tocris, 5148) in RPMI/B27- for another 2 days. Between 5–11 days of differentiation, RPMI/B27- media was used and changed every other day (switched to RPMI/B27+insulin after beating was observed). To improve the CM purity, cells were cultured in RPMI/B27+ without glucose, supplemented with 5 mM sodium L-lactate (Sigma Aldrich, 71718) for 3 days. On day 11, the iPSC-CMs were dissociated with TrypLE 10x (Thermo Fisher Scientific, A1217703) and seeded in 6-well Matrigel coated plates at a density of $2x10^6$ per well in RPMI/B27+ containing 10% KOSR and ROCK inhibitor Y-27632 (Tocris, 1253) (replating media). After 2 days, cells were cultured in RPMI/B27+ without glucose for 3 days prior to switch to 3ml of maturation media or RPMI/B27+. The sex of the iPSC-lines was not established.

iPSC-CMs media formulation

RPMI/B27 was composed in RPMI 1640 (Thermo Fisher Scientific, 11875119) with B27 supplement (Thermo Fisher Scientific, 17504-044). Maturation media was composed in DMEM without glucose (Thermo Fisher Scientific, 11966025) supplemented with 3mM glucose (Sigma Aldrich, G7021), 10mM L-lactate (Sigma Aldrich, 71718), 5μg/ml Vitamin B12 (Sigma Aldrich, V6629), 0.82μM Biotin (Sigma Aldrich, B4639), 5mM Creatine monohydrate (Sigma Aldrich, C3630), 2mM Taurine (Sigma Aldrich, T0625), 2mM L-carnitine (Sigma Aldrich, C0283), 0.5mM Ascorbic acid (Sigma Aldrich, A8960), 1x NEAA (Thermo Fisher Scientific, 11140), 0.5% (w/v) Albumax (Thermo Fisher Scientific, 11020021), 1x B27 and 1% KOSR (Thermo Fisher Scientific, 10828028).

METHOD DETAILS

Genome Editing in human iPSC

Human iPSCs were plated into Matrigel coated 6-well plates 1 day before transfection at low density in E8 media. On the day of transfection, the cells were supplied with E8 media supplemented with Rock inhibitor. The cells were transfected with Lipofectamine 3000 following manufacturer's instruction. 1 μg of CRISPR/Cas9 vector (pSpCas9(BB)-2A-GFP) and 4 μg of ssDNA donor were used for each well of a 6-well plate. GFP+ cells were isolated 36-48h after transfection using a FACSAria flow cytometer with a 100-μm nozzle. Cells were plated at density of 2-3*10^3 cells/well in a 6-well plate in E8 media supplemented with Rock inhibitor. Cells were

maintained in E8 media supplemented with Rock inhibitor for the first 3 days, then they were cultured in regular E8 media until the colonies reached a size of ~0.5 mm. Individual hiPSC clones were isolated with the assistance of a stereomicroscope located inside a cell culture cabinet and each re-plated in a well of a 24-well plate in E8 supplemented with Rock inhibitor. A few cells for each clone were resuspended in 20 μL media and used for genomic DNA isolation with 0.5 μL of DNA Release Additive in 20 μL Dilution Buffer (Phire Animal Tissue Direct PCR Kit (Thermo Fisher, F170S)). 2 μL of this mix was used for direct PCR amplification of the target genomic region using PrimeSTAR GXL DNA Polymerase (Clontech, R050B).

sgRNA design and cloning

The single guide RNA was designed using the Feng Zhang's lab CRISPR Design tool (https://zlab.bio/guide-design-resources). The two complementary oligonucleotides were ordered separately, annealed in T4 ligation buffer (NEB), and phosphorylated with T4 PNK (NEB). The annealed and phosphorilated oligos were cloned into the BbsI sites of the pSpCas9(BB)-2A-GFP plasmid (Ran et al., 2013) and transformed in STBL3 *E. coli* cells. The clones' sequence was confirmed by Sanger sequencing.
The oligos for the sgRNA cloning:

Fw_Guide2: CACCGCTCACCGGACTACGAGACCG
Rv_Guide2: aaacCGGTCTCGTAGTCCGGTGAGC

The lower-case letters represent the overhang nucleotides for the cloning.
The following sequence was used as donor:

> R634Q_KI_donor
TGTGGGACCTCGGGGAGAGTGACCGGCTCACCGGACTACGAGACtGCGGCCTTTCTGGGCCATATCTGTGAGGGAGCCAAG
GAGCAGGATTTAGAATCTTCACACCTCCCATCCCACCCCACCCACA

The lower-case letter represents the mutation.

Flow cytometry

For Edu incorporation experiment (Click-iT EdU Alexa Fluor 647, Thermo Fisher, C10424), hiPSC-CM were cultured for 4 days in media containing 10μM Edu prior to dissociation. For all flow cytometry experiments, hiPSC-CM were dissociated with TrypLE 10x, washed with D-PBS, stained with the fixable dead cells stain (ThermoFisher, L23105) according to the manufacturer's protocol, and then fixed with 4% paraformaldehyde. After washing with D-PBS, the cells were permeabilized in 1% BSA in D-PBS containing 0.1% (w/v) saponin (sigma) and incubated with primary antibodies (see Table S1) overnight in the permeabilization buffer. After washing, cells were incubated with secondary antibodies Alex Fluor 488 or 647 (Invitrogen) in permeabilization buffer for one hour. Edu detection was preformed according to the manufacturer's protocol. Cell sorting/flow cytometry analysis for this project was done on instruments in the Stanford Shared FACS Facility.

Western blots

For β-receptor stimulation experiment, hiPSC-CMs were exposed with 1μM isoproterenol (Tocris) for 15min prior to lyses. The cardiomyocytes were washed with cold PBS and lysed in RIPA buffer (Thermo Fisher, 89900) supplemented with 10X PhosStop (Roche, 4906845001) and 10X complete protease inhibitor (Roche, 11697498001) for 30 minutes on ice. BCA protein quantification was performed according to manufacturer's protocol and equal amount of protein was loaded and run on a precast 4%–20% gel (Biorad), followed by blotting of protein onto Trans-Turbo PVDF membrane (Biorad). Membraned were blocked in 5% BSA-TBS for one hour. After blocking the membranes were incubated with primary antibodies (see Key Resources Table) overnight while shaking at 4°C. After incubation with anti-mouse or anti-rabbit horseradish-coupled secondary antibody, the bands were visualized with FluroChem E (Protein Simple) imager.

Immunostaining

hiPSC-CMs were dissociated and seeded on Matrigel coated 12mm coverslips. After one week, cells were washed with PBS, fixed with 4% paraformaldehyde, and permeabilized in 5% BSA-PBS containing 0.3% triton. Cells were incubated with primary antibodies (see Key Resources Table) overnight at 4°C. After washing, cells were incubated with secondary antibodies Alex Fluor 488, 555, or 647 (Invitrogen) / Hoechst 33342, and mounted with Fluoromount-G (Southern Biotech). All images were collected on a Zeiss LSM 880 confocal system with a 40x/63x objective and using airyscan imaging mode, followed by airyscan processing using Zeiss Zen software.

qRT-PCR

Total RNA was extracted with a miRVana isolation kit (Thermo Fisher) and reverse-transcribed to cDNA with a QuantiTect reverse transcription kit (QIAGEN) according to the manufacturer's instructions. cDNA samples synthesized from 1 μg of total RNA were subjected to RT-qPCR with the 7900HT Fast real-time PCR system (Applied Biosystems) using the iTaq SYBR Green Supermix (Bio-Rad). Primer sequences are listed in Table S1. The data were analyzed with the ΔΔCt method, applying TBP as a normalization control (unless stated otherwise).

Fatty acid uptake assay

4 days prior to the assay, $2x10^4$ hiPSC-CMs were seeded on a Matrigel coated 384-well plate. The fatty acid was evaluated with the Free Fatty Acid Uptake Assay Kit (Abcam, ab176768) as recommended by manufacturer's protocol. Cells were washed 3x with serum-free media and preincubated in serum-free media for 2 hours. A baseline measurement was preformed prior to the addition of the fluorescent fatty acid mixture, and every 10 mins after the addition by using a microplate fluorescence reader at 485/528 nm(PerkinElmer, EnVision 2104).

Glucose assay

After three weeks of culture in either RPMI/B27 or MM, 10μl samples were taken from the hiPSC-CM culture (3mL total volume in well of 6-well plate) for four days following a media change. Glucose levels in the cell culture supernatant were determined using the glucose assay kit (Abcam, ab65333) as recommended by manufacturer's protocol. Fluorometric readout (Ex/Em = 535/587) was performed on plate reader (PerkinElmer, EnVision 2104).

Seahorse analysis

The Seahorse XF96 extracellular flux analyzer was used to assess mitochondria function. The plates were coated with Matrigel. The cardiomyocytes were seeded onto the plates with a density of 100,000 per XF96 well. Culture medium was exchanged for Agilent Seahorse XF DMEM Basal Medium supplemented with 2 mM glutamine, 10mM glucose and 1mM Sodium Pyruvate 1 hour before the assay and for the duration of the measurement. For the Mitro Stress test inhibitors were injected during the measurements as follows; oligomycin (2.5 μM), FCCP (2 μM), rotenone and antimycin A (2.5 μM). For the Glycolysis stress test; glucose (10mM), oligomycin (1 μM), and 2-DG (50mM). The oxygen consumption rate (OCR) and extracellular acidification rate (ECAR) values were normalized to the number of cells captured by one 10x field of view per well quantified by Hoechst staining. The baseline OCR was defined as the average values measured from time point 1 to 4 during the experiments. Maximal OCR was the OCR difference between uncoupler FCCP and (rotenone + antimycin A), with respiratory reserve capacity being the difference between FCCP and baseline OCR values.

RNA-seq

Total RNA was extracted with a miRVana isolation kit (Ambion) according to the manufacturer's instructions. Library prep and RNA sequencing was conducted by Novogene (20M reads per samples, PE150). FastQC (v0.11.5) and MultiQC (v1.3) were used to assess read quality. Adaptor and quality trimming of reads were performed with trimmomatic (v0.36). Reads were mapped to genome GRCh37 (hg19) using STAR (v2.5.3a) with UCSC gene annotations. Uniquely mapped reads were quantified with featureCounts (v1.28.1) from the Rsubread module. The DESeq2 Bioconductor package (v1.17.39) was used to identify genes that were differentially expressed between groups. Pairwise comparison between groups were conducted by applying the Wald test of the negative binomial distribution to the log2 gene counts and then Benjamini–Hochberg correction was applied.

Fura-2 measurements

Cardiomyocytes seeded on a glass coverslip for 5-7 days were loaded with the cell-permeable calcium sensitive dye fura-2 AM (2μM; abcam) for 20 minutes. After 5 minutes of washing in 1.8 mmol/L Ca-Tyrode buffer with 135mmol/L NaCl, 5.4mmol/L KCl, 1 mmol/L MgCl2, 5mmol/L glucose, and 10 mmol/L HEPES (pH 7.4) to allow de-esterification, coverslips were mounted on the stage of an inverted epifluorescence microscope (Nikon Eclipse Ti-S). After another 25 minutes of equilibration with 700uL of Ca-Tyrode buffer, myocytes were field stimulated at 0.5 Hz with pulse duration of 10 ms. Pacing was stopped after 10 s and 300uL of 50nM caffeine was added to induce full SR calcium release. Fura-2 AM loaded cells were excited at both 340 and 380 nm. The emission fluorescence signal was collected at 510nm(Lam et al., 2013). Changes in fluorescence signal were measured by the NIS Elements AR software, which permits recording of multiple cells in one view. Intracellular calcium changes were expressed as changes in ratio R = F340/F380 and the calcium transient waves were analyzed using the Greensmith's method (Greensmith, 2014). Diastolic calcium is indicated by the lowest F340/F380 signal. Transient amplitude is derived from subtracting the peak F340/F380 signal by the diastolic calcium level. Calcium removal rate constant indicates the rate of cytosolic calcium removal while calcium decay tau is a measure of the time required for cytosolic calcium removal.

Electrophysiology recordings

hiPSC-CMs were dissociated, plated in low density on Matrigel-coated coverslips and cultured in MM for 3-5 days before experiments. These coverslips with hiPSC-CMs were then transferred to a temperature-controlled chamber (Warner Instruments, Hamden, CT, USA) mounted on a Leica DMI3000 B inverted microscope (Leica Microsystems, Buffalo Grove, IL, USA), and continuously perfused (2 mL/min) with Tyrode solution containing (in mmol/L): NaCl 140, KCl 4, $CaCl_2$ 1.8, $MgCl_2$ 1, HEPES 5, Na-HEPES 5, and glucose 5.5; pH = 7.40. Patch-clamp experiments were performed in the whole-cell configuration. Electrodes were fabricated from borosilicate glass (World Precision Instruments, Sarasota, FL, USA) having tip resistances of 2-2.5 MΩ when filled with internal solution containing (in mmol/L): K-aspartate 100, KCl 30, NaCl 8, Mg-ATP 5, phosphocreatine-K_2 10, HEPES 10, EGTA 0.01, cAMP 0.002, and calmodulin 0.0001; pH = 7.20 (with KOH). Using this intracellular solution, the cells' spontaneous beating, intracellular Ca^{2+} transient and contraction were preserved. Axopatch 200B amplifier (Axon Instruments Inc., Union City, CA, USA) was used

for recordings, and the signals were digitized at 50 kHz by a Digidata 1322A A/D converter (Axon Instruments) under software control (pClamp10.4). The series resistance was typically 2-4 MΩ, and it was compensated by 90%. Experiments were discarded when the series resistance was high or increased by > 10%. Reported voltages are corrected for the liquid junction potential. All experiments were conducted at 37 ± 0.1°C. Action potentials (APs) were evoked by short depolarizing pulses (2-ms-long, 1.5x the threshold amplitude which allowed clear separation from the AP upstroke) generated by a Grass S44 external stimulator and delivered via the patch pipette. The intrinsic, spontaneous beating rate of all hiPSC-CMs studied was slower than 60 beats/min, which allowed us to record stimulated action potentials at 1 Hz pacing rate. Voltage-clamp experiments were performed to measure the inward rectifier K^+ current (I_{K1}). Tyrode solution was supplemented with 10 μmol/L tetrodotoxin and 10 μmol/L nifedipine to inhibit Na^+ and Ca^{2+} currents, respectively. I_{K1} current–voltage relationships were obtained by plotting the magnitude of the Ba^{2+}-sensitive I_{K1} traces measured at the end of the 500 ms test pulse as a function of the test depolarization, arising from the holding potential of −80 mV. I_{K1} magnitude were normalized to cell capacitance (I_{K1} density), determined in each cell using short (10 ms) hyperpolarizing pulses from −10 to −20 mV. Cell capacitance was 56.8 ± 3.1 pF (n = 44 cells).

We recorded I_{Na} using whole cell ruptured patch clamp at room temperature. Bath solution contained CsCl 4 mM, $MgCl_2$ 1 mM, $CaCl_2$ 2 mM and either 140 mM NaCl or 30 mM NaCl + 110 mM NMG-Cl, with pH set to 7.4 using HEPES free acid and Na salt. Pipette solution contained TEA-Cl 20 mM, with $MgCl_2$ 5.6 mM + EGTA 5 mM + $CaCl_2$ 2.63 mM + calmodulin 1 μM + ATP-Tris 5 mM, (free [Ca] near 0.2 μM and free [Mg] near 1 mM), GTP-Li 0.3 mM, and NMG 105 mM, titrated to pH 7.2 with free glutamic acid. Cells were held at −140 mV to maximize initial I_{Na} availability and depolarized for 40 msec. Voltage clamp steps (E_m) were sized to bracket the range from 0 to maximal activation. The liquid junction potential (9 mV, pipette negative) was corrected and series resistance was compensated as needed for voltage control. We fit peak I_{Na} versus E_m (after subtracting nonspecific leak current from all data) to a Boltzmann activation function $I = G_{max} / (1 + \exp((V_{50} - E_m) / k)) * (E_m - E_{rev})$, where Gmax (conductance at maximal activation), V_{50} (E_m at half maximal activation), k (slope factor representing channel sensitivity to changes in E_m) and E_{rev} (E_m at which current reverses) are the fit parameters. Removing the driving force factor ($E_m - E_{rev}$) and normalizing by G_{max} yielded activation probability.

Dynamic Monolayer Force Microscopy (DMFM)

We applied Dynamic Monolayer Force Microscopy(Banerjee et al., 2015; Lamason et al., 2016) to quantify the traction forces applied by a confluent cell sheet on their substratum and the cumulative mechanical stresses transmitted through the cell sheet. In brief, hiPSC-CMs were plated on polyacrylamide gel substrates with nominal Young's modulus E = 8.73kPa. The gels were seeded with 0.2 μm TRITC fluorescent beads (FluoSpheres; Thermo Fisher) and their surface was coated with matrigel. The kinetic image cytometer (KIC) was used with 20x magnification to acquire time-lapse sequences of 6 s duration at 100 Hz acquisition rate. As the cells contracted, they generated deformations in their substratum, which were measured by tracking the motion of the fluorescent beads using Particle Image Velocimetry with a window size of 64x64 pixels with 32 pixel overlap. The traction stresses were determined from the measured deformations by solving the partial differential equations of equilibrium for the polyacrylamide substratum, which behaved like a linearly elastic medium, as previously described (Del Alamo et al., 2007). Dynamic analysis of the deformation allowed for the traction stresses to be determined during several contraction cycles without removing the cells from the gels. The cumulative intracellular stresses transmitted through the cell sheet were determined by solving the Kirchhoff–Love equations of mechanical equilibrium for a thin elastic plate subject to the forcing created by the measured traction stresses, using previously described methods (Serrano et al., 2019; Tambe et al., 2013). Overall intracellular stress was quantified for each sample by spatially averaging the maximum principal value of the intracellular stress at the instant of peak contraction.

Kinetic Image Cytometer (KIC)

For all experiments, hiPSC-CMs were plated on Matrigel at 20,000 cells per well of a 384-well plate (Greiner Bio-One) in 50 μl of replating media. The subsequent day an additional 50 μl of normal media was added and cells were grown for a minimum of 3 days prior to analysis. If applicable, siRNAs were added one day after replating at 20nM concentration with 0.1 μl Lipofectamine RNAiMax (Invitrogen) per well. For the analysis, hiPSC-CMs were removed from a 37°C 5% CO_2 incubator and placed immediately into in a tissue culture cabinet on a dry heat block set to 37°C to prevent temperature fluctuation during the subsequent washing and dye loading steps.

Calcium assay

50 μl of media was removed form 384-well plates and 50 μl 2x Fluo-4 (Invitrogen) with Hoechst 33258 (Life Technologies) in FluoroBrite DMEM (GIBCO) was added as recommended by manufacturer's protocol. After 40min incubation in a 37°C 5% CO_2 incubator, cells were washed by removing 50 μL of media and replacing it with 50 μL FluoroBrite solution four times. After 10min recovery, 50 μL of solution was removed and 50 μL of 2x reference compound was added to the respective well and incubated at 37°C and 5% CO_2 for 5 min before image acquisition. Time series images were acquired automatically using the IC200 KIC instrument (Vala Sciences, San Diego, USA) at an acquisition frequency of 33Hz for a duration of 10 s.

Voltage assay (McKeithan et al., 2017)

cells were washed 4 times as described above with FluoroBrite and 50 μL of the 2x VF2.1.Cl dye loading solution was added to each well. The plate was placed back in the 37°C 5% CO_2 incubator for 50 min. Cells were further processed for analysis in the same manner as the calcium assay. Voltage time series were acquired at frequency of 100Hz for a duration of 10sec.

Contractility assay

50μl of media was removed form 384-well plates and 50μl imaging dye (wheat germ agglutinin–Alexa Fluor 488 conjugate (5 μg/ml; Life Technologies) and Hoechst) in Fluorobrite was added and incubated at 37°C and 5% CO_2 for 10 min. Cells were further processed for analysis in the same manner as the calcium assay. Contractile time series were acquired at frequency of 100Hz for a duration of 6.5sec. The contractility image analysis and physiological parameter calculation were conducted as previously described (Sharma et al., 2017). The voltage and calcium image analysis and physiological parameter calculation were conducted using commercially available Cyteseer (Vala Sciences) as previously described (Cerignoli et al., 2012). The metrics analyzed by the whole well cardiac time series algorithm were APD_{25}/CTD_{25} and APD_{75}/CTD_{75}, (referring to the width of the cardiac action potential (ADP) or the calcium transient duration (CTD) at a point 25 and 75, respectively).

Generation and culture of EHTs with hiPSC-CM

The human induced pluripotent stem cell lines were from skin biopsies of two healthy female volunteers of the *ERC IndivuHeart* project (See certificates, hPSCreg: UKEi001-A/ERC001sv1162; hPSCreg: UKEi003-C/ERC018sv1634). This investigation conforms to the principles outlined by the Declaration of Helsinki and the Medical Association of Hamburg. All materials from patients were taken with informed consent of the donors. All procedures involving the generation and analysis of hiPSC lines were approved by the local ethics committee in Hamburg (Az PV4798, 28 October 2014). Cardiac differentiation and generation of EHTs with hiPSC-CM was conducted according to the recently published in-house standardized protocol (Breckwoldt et al., 2017). Three differentiation runs were cast to Engineered Heart Tissues with each 1 Mio hiPSC-CM embedded in fibrin hydrogel (EHTs). Two differentiation runs were cast of UKEi001-A/ERC001sv1162 (batch 1 and 3) and one differentiation run was cast of UKEi003-A/ERC018sv1634 (batch 2). In this experiment we compared our standard EHT horse serum-based culture medium (Complete; DMEM (Biochrom, cat. no. F0415), heat-inactivated horse serum (10% (vol/vol); Life Technologies, cat. no. 26050088), penicillin/streptomycin (1% (vol/vol); GIBCO, cat. no. 15140), aprotinin (0.1% (wt/vol); 33 μg/ml; Sigma-Aldrich, cat. no. A1153), and insulin (0.1% (wt/vol); 10 μg/ml; Sigma-Aldrich, cat. no. I9278)) with maturation media.

Analyzes of EHTs

Analysis of contractile force of EHTs by video-optical recording (EHT Technologies) was conducted as previously described (Hansen et al., 2010). Functional analyzes were also recorded video-optical with additional electrical stimulation of EHTs by graphite electrodes as previously described by Mannhardt et al. (2016). For histological analyzes EHTs were fixed without prior relaxation. For paraffin sections EHTs were fixed in formaldehyde (4% Roti®-Histofix, Carl Roth, P087.3) and stained with antibodies for MLC2a and MLC2v. For immunofluorescence EHTs were also fixed in formaldehyde and stained with α-actinin (Thermo Fischer Scientific, PA5-16891 and A11008) und Hoechst (Invitrogen, H3569). Quantification of sarcomere length and EHT width and length was conducted utilizing ImageJ. For electron microscopy EHTs were fixed in 4% Paraformaldehyde with 1% Glutaraldehyde (Science Services, Deutschland). For metabolic analysis glucose and lactate concentrations from media samples, taken at different time points after medium change, were measured with a blood gas analyzer (Radiometer ABL90 SERIE, Radiometer GmbH). For analyzes of DNA and protein TRIzol isolation was performed according to the manufacturer's instructions. To study the ratio of mitochondrial DNA content (NADH-dehydrogenase 1 (ND1) and NADH-dehydrogenase 2 (ND2)) to genomic DNA content (g-actin) for metabolic processes a quantitative realtime PCR was done. Blood gas and DNA content analyzes were conducted as previously described by Ulmer et al. (2018). Protein analyses were done by western blotting as previously described (Pohlmann et al., 2007). Each sample was loaded once on two gels to detect α-MHC (224 kDa, rabbit polyclonal, Theresia Kraft (Hannover), 1:1000; anti-rabbit IgG, Sigma A0545 (1:5000)) and β-MHC (220 kDa, mouse monoclonal, Sigma M-8421 (1:4000); anti-mouse IgG Sigma A9044 (1:5000). The positive control was an in-house non-failing heart sample and the negative control neonatal ventricular cardiomyocytes of a rat EHT protein sample. α-MHC and β-MHC was quantified by normalization to cTNT and then to the Complete EHTs per batch.

QUANTIFICATION AND STATISTICAL ANALYSIS

Data are presented as mean ± standard error of the mean (SEM) as indicated. Statistical analysis was conducted using GraphPad Prism version 8.0.2. Significance was calculated using the two-tailed unpaired Student's t tests. Data that were not normally distributed were tested using the Mann–Whitney–Wilcoxon test. One-way ANOVA with Dunnett's method was used for multiple comparisons. A p value < 0.05 was considered statistically significant.